Materials Advances

ROYAL SOCIETY OF CHEMISTRY

PAPER

View Article Online
View Journal

Check for updates

Cite this: DOI: 10.1039/d6ma00528d

Modulation of oxygen vacancies influences the electrocatalytic performance of Ni-doped ceria for oxygen and hydrogen evolution

Ajit Kumar Dhanka,[a] Mayank Tiwari,[b] Prashant K. Bhartiya,[c] Balaram Pani,[d] Avneesh Mittal,[e] Debabrata Mishra*[b] and Nityananda Agasti*[a]

Received 15th April 2026,
Accepted 30th April 2026

DOI: 10.1039/d6ma00528d

rsc.li/materials-advances

The development of high-performance catalysts for electrochemical water splitting continues to drive advancements in sustainable hydrogen production. With ceria-based materials being potential catalysts owing to their remarkable redox behaviour, modulation of defects in ceria is an effective strategy for efficient electrocatalytic water splitting. Thus, aiming to study the creation of oxygen vacancies as a function of dopant concentration, this report demonstrates enhanced electrocatalytic water splitting by regulating defects in ceria *via* nickel doping. Nickel-doped ceria acts as a bifunctional electrocatalyst with enhanced activity for both oxygen and hydrogen evolution. This improvement stems from interfacial interactions between Ni and the CeO_2, which enhances oxygen vacancy defects in ceria. Mechanistic insights derived by a range of spectroscopic techniques reveal an enhancement in oxygen vacancies in ceria with the increase in the concentration of the dopant. Photoluminescence (PL) studies reveal suppressed charge recombination, indicating efficient electron–hole separation facilitated by the defects. The defect regulated electrocatalytic performance has been established *via* the electrocatalytic hydrogen evolution reaction (HER) and oxygen evolution reaction (OER) with the evolution of H_2 and O_2 quantitatively estimated, using Ni-doped CeO_2 and undoped CeO_2. Notably, doping of Ni results in a significant reduction in overpotential by 87 mV for oxygen evolution and 59 mV for hydrogen evolution. In addition, current densities also experience a substantial increase by 166 mA cm^{-2} for oxygen evolution and 96 mA cm^{-2} for hydrogen evolution. The reduction in the Tafel slope from 381 to 199 mV dec^{-1} for the OER and from 334 to 217 mV dec^{-1} for the HER indicates faster reaction kinetics. Chronoamperometric measurement reveals notable electrochemical stability of the Ni-doped CeO_2 electrocatalyst. This study on defect structure-related electrocatalysis provides insight into the dopant regulated defect generation in ceria-based materials for designing electrocatalysts for effective water splitting.

1. Introduction

Fossil fuels such as coal, natural gas, and petroleum have long been crucial in fulfilling global energy requirements, supporting industries, transportation, and daily life. However, the growing global population and rapid industrialization have led to an overreliance on these non-renewable resources, raising concerns about future shortages.[1,2] Experts predict that crude oil reserves may be exhausted within 40 to 50 years,[3] coal production is expected to peak between 2042 and 2062,[4] and the demand for clean energy is projected to increase by 50% by 2030.[5] Given these challenges, hydrogen has emerged as a promising alternative energy source due to its high energy yield and zero carbon emissions.[6–8] One of the most economical methods for producing hydrogen is steam reforming; however, it faces significant environmental challenges. These include the formation of significant amounts of carbonaceous byproducts, expensive methods, severe reaction conditions, and the dependence on an external heat transfer system to maintain the reaction.[9–11] Additionally, producing 1 kilogram of hydrogen releases nearly 9 kilograms of carbon dioxide.[12] A more sustainable approach is electrochemical water splitting,[13] which involves two key reactions: the hydrogen

---

[a] Department of Chemistry, University of Delhi, North Campus, Delhi 110007, India. E-mail: nnagasti@chemistry.du.ac.in
[b] Department of Physics and Astrophysics, University of Delhi, North Campus, Delhi 110007, India
[c] Delhi School of Climate Change and Sustainability, Institution of Eminence, University of Delhi, Delhi 110007, India
[d] Department of Chemistry, Bhashkaracharya College of Applied Sciences, University of Delhi, Dwarka, New Delhi, 110075, India
[e] Department of Electronic Sciences, Bhaskaracharya College of Applied Sciences, University of Delhi, Dwarka, New Delhi, 110075, India

evolution reaction (HER) to generate hydrogen and the oxygen evolution reaction (OER) to produce oxygen.[14–16] Despite its potential, the efficiency of this method is hindered by high overpotentials, sluggish reaction kinetics, and the need for cost-effective and durable catalysts.

Recent research has focused on semiconductor metal oxides as promising electrocatalysts for water splitting.[17–23] Among these, cerium oxide (CeO_2) has gained significant attention due to its exceptional redox properties, attributed to the coexistence of Ce^{3+} and Ce^{4+} oxidation states. This redox behavior facilitates the creation of oxygen vacancies in the CeO_2 lattice, represented as $Ce^{4+}–O_v–Ce^{3+}$ (where O_v denotes an oxygen vacancy). These vacancies enhance the catalytic performance of CeO_2 in various electrochemical applications.[24,25] Additionally, CeO_2 is an n-type semiconductor with a band gap of around 3.2–3.3 eV.[26] However, its wide band gap presents a limitation; the density of reactive charge carriers is insufficient for the electrocatalytic reaction.[27] This necessitates the development of band gap-engineered ceria nanostructures with tailored electronic properties to enhance their suitability for electrocatalytic applications.[28–30] Recent advancements in ceria-based nanomaterials have focused on tuning the band gap and increasing surface defects to enhance light absorption and to minimize recombination of photogenerated electron (e^-) and hole (h^+) pairs. Ghosh *et al.* have demonstrated that incorporating defects into ceria heterojunction catalysts significantly improves their performance in hydrogen evolution. The improvement arises from their ability to capture a wider portion of the visible spectrum, facilitate more effective separation and migration of charge carriers, and adjust the electronic structure to favor the reaction process.[31] Our research group has recently demonstrated that incorporating silver into the ceria lattice effectively generates oxygen vacancies *via* defects, which in turn leads to a marked improvement in overall water-splitting performance.[32] Furthermore, CeO_2 serves as an effective catalyst support, enabling the integration of metal or metal oxide nanoparticles (NPs) to form heterojunctions. The introduction of metal nanoparticles onto ceria (CeO_2) surfaces forms well-defined metal–ceria interfaces, which are known to enhance interfacial charge transfer and thereby improve electrocatalytic performance in water-splitting reactions. These interfaces enhance electrical conductivity and catalytic activity by modifying the electronic structure of ceria and stabilising reactive intermediates. Among commonly used transition metals such as Ag, Au, Cu, Fe, and Ni, Ni stands apart due to its strong metal–support interaction with ceria.[33–38] Doping Ni into ceria significantly increases the density of surface oxygen vacancies. These vacancies serve as critical active sites that enhance the water-splitting kinetics. Furthermore, the doped Ni modifies the electronic band structure of ceria by reducing its band gap, thus facilitating improved electrical conductivity and charge transport under electrochemical operating conditions.[39,40] Notably, Ni is a ferromagnetic material, and its magnetic properties also contribute to the formation of triplet-state molecular oxygen ($^3O_2$) during the OER. Ni could provide a pool of spin-polarized electrons, which promotes the formation of $^3O_2$ by lowering the energy barrier required for the formation of triplet oxygen.[41–43] Thus, Ni doping in ceria can introduce a combination of (i) structural defects (oxygen vacancies), (ii) electronic modifications (band gap narrowing), and (iii) spin-related phenomena (triplet O_2 generation), all of which can synergistically improve the electrocatalytic activity of ceria for water splitting reactions.

Though ceria-based catalysts have been studied for energy applications, comprehensive investigations into the nature of defects within ceria and their influence on electrocatalytic performance, especially in the OER and HER, remain scarce. Most existing literature offers limited insight into the detailed structural analysis of these defects and their direct mechanistic contributions to catalytic performance.[44–47] Therefore, this study aims to address these gaps by providing an in-depth examination of the structural defects in ceria-based materials and exploring their specific roles in enhancing the water splitting kinetics. Furthermore, there has been very limited study on the effect of the concentration of oxygen vacancies on electrocatalytic activities of ceria-based materials. To address this gap, herein we attempt to investigate the defect-dependent electrocatalytic performance of ceria-based materials. We have synthesized Ni-doped CeO_2 *via* a solvothermal method with varying nickel concentrations (1%, 5%, and 10%), to study their electrocatalytic performance for water splitting. Compared to pristine CeO_2, the Ni-doped CeO_2 samples exhibit progressively improved electrocatalytic activity with increasing concentration of Ni, owing to (i) enhanced defect formation, (ii) improved charge transfer, and (iii) a greater density of active surface sites. Among all samples, the 10% Ni/CeO_2 catalyst exhibits the most optimized electrocatalytic performance, achieving a notable reduction in the overpotential of 87 mV for the OER and 59 mV for the HER compared to pristine CeO_2. Additionally, it shows substantial improvements in current density, with a 66% enhancement for the OER and a 140% enhancement for the HER. This enhancement highlights the crucial role of Ni concentration in tuning the electrocatalytic efficiency of ceria-based systems. Furthermore, characterization studies reveal that Ni incorporation induces defect states and lattice expansion due to charge imbalance, stemming from the variable oxidation states of Ni. These defects increase surface oxygen vacancies, which act as electron traps, suppressing recombination and promoting charge carrier separation. Additionally, the band gap decreases progressively with Ni content: from 3.31 eV for CeO_2 to 3.23, 3.11, and 3.03 eV for 1%, 5%, and 10% Ni-doped CeO_2, respectively. The synergistic interaction between Ni and CeO_2 enhances the structural and electronic properties of Ni-doped CeO_2, thereby improving its overall electrocatalytic activity. A plausible reaction pathway is proposed to elucidate the mechanistic role of Ni-doped CeO_2 in facilitating both hydrogen and oxygen evolution, emphasizing the significance of doped metal and ceria interactions in advancing next-generation catalysts for sustainable hydrogen production.

2. Experimental section

2.1. Materials

During this research, all reagents used were commercially available and utilized without any further purification. Cerium nitrate hexahydrate ($Ce(NO_3)_3\cdot 6H_2O$, 99%), sodium hydroxide (NaOH, 98%), ethanol (C_2H_5OH), methanol (CH_3OH), nickel foam (NF), potassium hydroxide (KOH), polyvinylidene fluoride (PVDF), carbon black, and methanol (CH_3OH) were procured from Sigma-Aldrich India, while nickel nitrate hexahydrate ($Ni(NO_3)_2\cdot 6H_2O$) was obtained from Merck India.

2.2. Preparation of Ni-doped CeO_2

The Ni-doped CeO_2 was synthesized by a solvothermal method[48], using cerium nitrate ($Ce(NO_3)_3\cdot 6H_2O$) and nickel nitrate ($Ni(NO_3)_2\cdot 6H_2O$) as precursors. In a typical preparation method, cerium nitrate and nickel nitrate were dissolved in 50 mL of methanol. The mixed solution was kept under constant magnetic stirring to make it homogeneous. 0.25 g of sodium hydroxide dissolved in 10 ml of methanol in a separate beaker was added dropwise into the mixed solution with continuous stirring for 30 minutes. After being stirred, the mixed solution was transferred into a Teflon-lined stainless-steel autoclave and heated for 18 hours at 180 °C in an oven. On naturally cooling the autoclave to room temperature, the obtained colloidal solution was centrifuged at 8000 rpm for 5 minutes and washed with ethanol 3–4 times. Finally, the precipitate obtained was dried at 80 °C overnight and subsequently calcinated at 250 °C for 2 hours to obtain Ni-doped CeO_2 (Ni/CeO_2). To study the effect of Ni concentration on the defects in CeO_2, Ni-doped CeO_2 was prepared with varied concentrations of Ni; 1% (6.6 mg), 5% (33.4 mg), and 10% (66.8 mg) (Ni $(NO_3)_2\cdot 6H_2O$) was mixed into (1.0 g) Ce $(NO_3)_3\cdot 6H_2O$. For comparison, CeO_2 nanoparticles were prepared by the same procedure, except without the addition of nickel nitrate.

2.3. Fabrication of electrodes for electrochemical measurements

The electrodes were fabricated using the drop-casting method, where CeO_2 and Ni/CeO_2 were applied onto nickel foam (NF). The first electrode was prepared by drop-casting CeO_2 as the active material, polyvinylidene fluoride (PVDF) as the binder, and carbon black as the conducting agent in a ratio of 85 : 10 : 5, respectively. Similarly, additional electrodes were prepared using Ni/CeO_2, maintaining the same composition ratio. To study the effect of varied concentrations of the dopant (Ni) on the electrocatalytic performance, electrodes were prepared with Ni/CeO_2 with Ni concentrations of 1%, 5%, and 10%. The Ni/CeO_2 materials were coated onto the nickel foam, covering an area of 1 cm^2 using the drop-casting technique. After coating, the electrodes were placed in a vacuum oven at 80 °C for 10 hours to ensure proper drying, followed by natural cooling to room temperature. The fabricated electrodes were designated as NF (bare nickel foam), NF/CeO_2 (CeO_2-coated on nickel foam), NF/1% Ni/CeO_2 (1% Ni doped CeO_2 coated on nickel foam), NF/5% Ni/CeO_2 (5% Ni doped CeO_2 coated on nickel Foam), and NF/10% Ni/CeO_2 (10% Ni doped CeO_2 coated on nickel foam).

2.4. Sample characterization

To study the structural and morphological features of the synthesized materials, multiple characterization techniques were considered. Ni/CeO_2 and CeO_2 were characterized by powder X-ray diffraction (PXRD) to understand the crystalline pattern of the composites using an FEI Quanta 200 F SEM diffractometer with Cu K radiation (λ = 0.1542 nm) in the 2θ range of 20–80. To understand the optical behavior of the materials, UV-visible absorbance spectra were recorded using a Shimadzu 1800 Spectrophotometer, and UV-vis diffuse reflectance spectra (DRS) using an Agilent Cary 5000. Raman spectroscopy (Laser Raman Spectrometer Model Invia II) was carried out to study defects in the materials. The morphological character of the Ni/CeO_2 and CeO_2 was examined using Field Emission Scanning Electron Microscopy (FESEM) with an Oxford-EDX system IE 250 X Max 80 (FEI Quanta 200 F SEM). The elemental composition of the samples was analyzed by Energy Dispersive X-ray spectroscopy (EDX). Moreover, to gain a thorough insight into the packing pattern of Ni/CeO_2, high resolution transmission electron microscopy (HRTEM) images were collected using a TECNAI G20 HR-TEM 200 kV transmission electron microscope. Thermogravimetric analysis (TGA) was performed on a HiRes1000 from RT to 1100 °C with a heating rate of $10^\circ\ min^{-1}$ to determine the thermal stability of the materials. Surface area, pore size and pore volume were analyzed by the Autosorb-iQ XR system (Quantachrome Instruments). Before measurement, the samples underwent degassing at 150 °C for 10 hours under high vacuum conditions ($\sim 1 \times 10^{-5}$ bar) to eliminate any physiosorbed contaminants. The adsorption–desorption isotherms were then acquired at 77 K using liquid nitrogen to maintain a stable cryogenic environment for precise analysis. The surface elemental oxidation state and composition were analyzed by X-ray photoelectron spectroscopy (XPS) using a Kratos Axis Supra Plus *XPS* equipped with a monochromatic Al Kα X-ray source (1486.6 eV). The high-resolution data were charge corrected to the reference C 1s signal at 284.5 eV. The photoluminescence (PL) analysis was performed under ambient conditions using a Horiba Yvon PTI QuantaMaster (8450-11) spectrophotometer, where a nano-LED was utilized as the excitation light source. The electron spin resonance (ESR) spectra of the powdered samples were obtained using a JEOL JES-X320 X-band spectrometer operating at room temperature. The measurements were performed under the following conditions: a microwave frequency of 9.17 GHz, modulation frequency of 100 kHz, scan range of 1300 mT, and center field of 3270.00 G. Electrochemical measurements, including Linear Sweep Voltammetry (LSV), electrochemical impedance spectroscopy (EIS), and chronoamperometry, were performed in an alkaline medium using a CS350 Corr-Test electrochemical workstation (Potentiostat) under a standard three-electrode configuration. A platinum (Pt) electrode served as the counter electrode, while an Ag/AgCl electrode was the reference electrode. To ensure consistency in potential values, they were converted to the reversible hydrogen electrode (E_{RHE}) using the Nernst equation.[49] All electrochemical measurements were performed in a 1 M KOH solution, which served as the electrolyte. The quantification of hydrogen (H_2) and oxygen (O_2) gases was conducted in a tightly sealed Hoffmann apparatus.

3. Results and discussion

3.1. Structure, morphology and elemental analysis

The prepared Ni-doped CeO_2 (Ni/CeO_2) and CeO_2 were analyzed using UV-vis absorption spectra (Fig. 1a). The band observed at a wavelength of 301 nm is characteristic of CeO_2 nanoparticles.[50] However, in the spectrum of the doped CeO_2, with increased concentration of Ni dopant, the band shifts towards the visible region. It exhibits a red shift in the absorption band from 301 nm to 323 nm due to the absorption edge induced by the incorporation of Ni[51] (Fig. S1, SI). The peak shifting in doped CeO_2 indicates a decrease in the band gap and crystallite size.[52–54] Furthermore, the interaction of Ni with the ceria lattice induces the formation of oxygen vacancies and enhances the reduction of Ce^{4+} to Ce^{3+}. The increased presence of Ce^{3+} species gives rise to localised electronic states that emerge near the conduction band, which ultimately leads to a reduction in the energy band gap in doped ceria.[55] The direct energy band gap (E_g) of Ni/CeO_2 and CeO_2 was calculated using UV-vis diffuse reflectance spectroscopy (DRS) using the Kubelka–Munk (K–M) function. To minimize the effects of light scattering in the DRS spectra and ensure accurate band gap measurements for solid materials, the Kubelka–Munk (K–M) function was utilized. The band gap plot obtained from the K–M function relates to the energy of the photons. The E_g values for CeO_2 and Ni-doped CeO_2 were specifically determined from the point where a linear fit of the Kubelka–Munk function intersects the abscissa axis, using the equation:

$$\alpha h\nu = A(h\nu - E_g)^{n/2}$$

where α is the absorption coefficient, A is a constant, h is Planck's constant, ν denotes the frequency of light, and E_g corresponds to the band gap energy.[56] The DRS spectra reveal that the estimated band gap energies (E_g) are 3.03, 3.11, 3.23 and 3.31 eV for 10%, 5%, 1% Ni/CeO_2 and CeO_2, respectively (Fig. 1b). The observed reduction in band gap in Ni-doped CeO_2 can be attributed to the incorporation of Ni in the CeO_2 lattice facilitating electron excitation from the conduction band to the valence band, which is consistent with the findings in the literature.[57,58] Also, the incorporation of Ni ions leads to the creation of interstitial sites, because Ni^{2+}/Ni^{3+} ions replace Ce^{4+} in the CeO_2 lattice. These interstitial sites introduce defect or impurity energy levels between the valence and conduction bands of CeO_2, facilitating the electron transition.[59]

To confirm the formation of Ni-doped CeO_2 from structural characteristics, powder X-ray diffraction (PXRD) analysis was conducted in the 2θ range of 20 to 80°. The eight peaks observed at 2θ angles 28.4, 32.9, 47.5, 56.3, 59.0, 69.3, 76.7, and 78.8 correspond to the (111), (200), (220), (311), (222), (400),

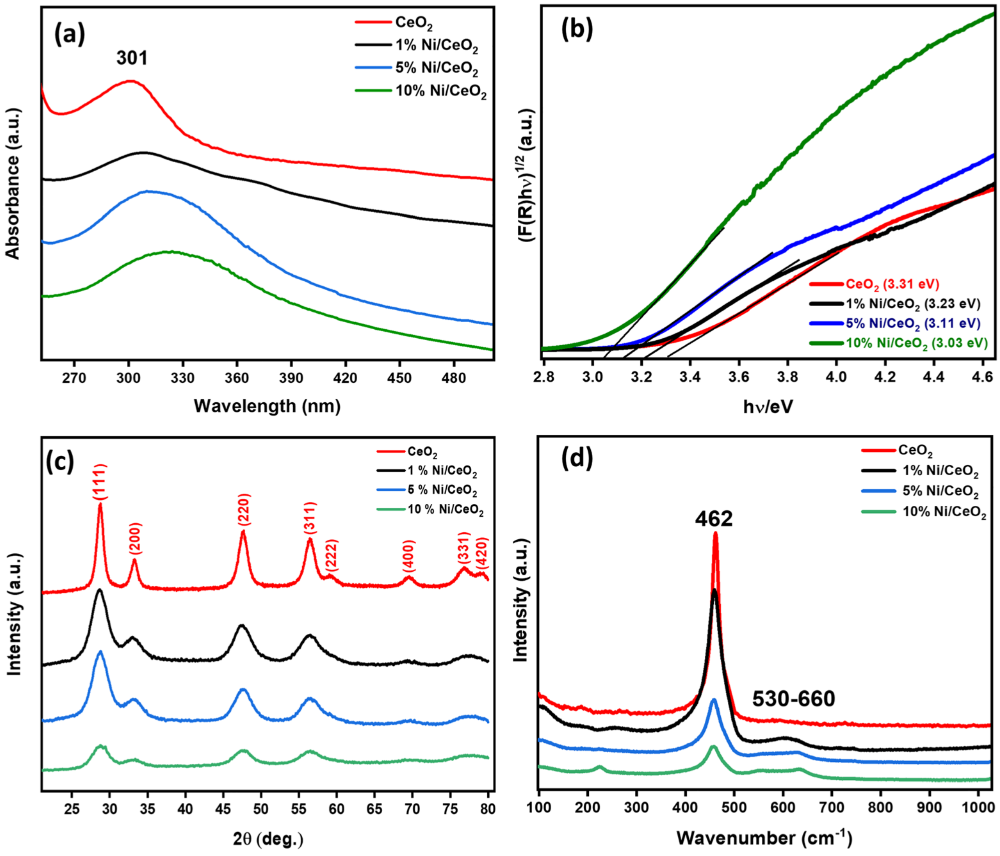

Fig. 1 (a) UV-vis absorption spectra, (b) calculated band gap energy using UV-Vis DRS by the Kubelka–Munk (K–M) function, (c) PXRD spectra and (d) Raman spectra for CeO_2 and 1, 5 and 10% Ni/CeO_2.

(331), and (420) planes of CeO_2 crystals (Fig. 1c). The sharpness of these XRD peaks in the synthesized nanoparticles indicates the formation of a crystalline phase with no impurities or secondary phases detected within the instrumental limits and these peaks match with the cubic fluorite structure of CeO_2 (JCPDS card data 34-0394).[60] No additional diffraction peak Ni was observed after the addition of Ni into CeO_2. However, there is a decrease in the peak intensity and broadening of the peaks, on increasing the concentration of the dopant (1, 5 and 10%) Ni in CeO_2 (Fig. S2a, SI). This indicates the formation of crystal defects around the dopant atoms. Also, the substitution of Ni ions appears to have inhibited the growth of CeO_2 nanoparticles and thus degraded their crystal quality.[61] Moreover, there is a reduction in crystallite size, which is evident from the change in full-width at half-maximum (FWHM).[62] Compared to pristine CeO_2, the FWHM of the (111) peak is higher in Ni-doped ceria. Furthermore, in Ni-doped CeO_2, the FWHM of the (111) peak increases with an increase in the concentration of Ni. This suggests that the incorporation of Ni into the CeO_2 lattice can be attributed to the creation of defects in doped ceria.[63] Besides an increase in the FWHM, there is a slight downshift of the (111) peak in Ni-doped CeO_2 compared to pristine CeO_2 (Table 1). The crystallite size of pristine ceria and doped ceria was estimated using the Scherrer equation,[64] $D = K\lambda/\beta\cos\theta$, where D represents the crystallite size, K is a dimensionless shape factor, often taken as 0.98 for spherical crystals, λ denotes the wavelength of the X-rays (typically 1.54 Å for copper Kα radiation), β is the full-width at half-maximum (FWHM) of the (111) peak and θ is the Bragg angle (half of the 2θ angle where the peak occurs). The crystallite size of ceria was calculated to be 8.35 nm for pristine CeO_2 nanoparticles and 3.77, 3.67 and 3.66 nm for 1, 5 and 10% of Ni-doped CeO_2, respectively.

Additionally, on incorporation of Ni of concentration up to 10% into CeO_2, the X-ray diffraction (XRD) patterns typically show no extra peaks, indicating that Ni ions are successfully integrated into the CeO_2 matrix without forming separate phases. This suggests substitutional doping of Ni into the CeO_2 lattice and the formation of a single-phase material. However, when the concentration of Ni exceeds 10%, diffraction peaks corresponding to NiO begin to appear,[65] indicating the formation of a secondary phase (NiO) in addition to the CeO_2 structure,[66] which is shown in Fig. S2b and c, SI.

Raman spectroscopy is a non-destructive technique used to characterize nanomaterials and the defects in them. So, to ascertain the oxygen vacancies formed in CeO_2 due to Ni doping, the Raman spectra of CeO_2 and Ni-doped CeO_2 were measured in the range of 100–1020 cm^{-1} as shown in Fig. 1d. Pristine CeO_2 typically exhibits a prominent Raman peak at 462 cm^{-1}, corresponding to the Raman-active vibrational mode (F_{2g}), a characteristic of the fluorite structure.[67] 1, 5, and 10% Ni doped CeO_2 displayed a strong Raman peak in this region, confirming the preservation of the fluorite structure of ceria. Additionally, the appearance of the bands in the region 530–660 cm^{-1} corresponds to a defect-induced mode (D),[68] which is associated with the oxygen vacancies[56] (Fig. S3b, SI). The D bands (highlighted with a pink region), which are not so prominent in the pristine CeO_2, indicate an increase in oxygen vacancies with an increase in the concentration of the dopant Ni. Moreover, the intensity of the characteristic F_{2g} peak for Ce–O at 462 cm^{-1} decreases with an increase in the concentration of the dopant, Ni in CeO_2. Besides, the F_{2g} peak also suffers a downshift towards lower wavenumbers from 462 cm^{-1} (CeO_2) to 458 cm^{-1} for 10% Ni-doped CeO_2 (Fig. S3a, SI). The decrease in intensity and downshift of the F_{2g} peak suggest an increase in oxygen vacancies in Ni/CeO_2. The increase in oxygen vacancies in CeO_2 is represented by an increase in Ce^{3+} concentration. Compared to pristine CeO_2, there is an increase in Ce^{3+} in Ni-doped CeO_2, which is also confirmed from the expansion of the crystal lattice. The incorporation of dopant Ni has led to an increase in the concentration of Ce^{3+} ions in ceria, resulting in a notable expansion of the crystal lattice. This expansion is attributed to the larger ionic radius of Ce^{3+} compared to Ce^{4+}.[69] The lattice expansion is further evidenced by the observed decrease in the full width at half maximum (FWHM) of the F_{2g} peaks in doped CeO_2. This reduction in FWHM indicates an increase in crystallite size, which is consistent with the lattice expansion caused by the higher proportion of Ce^{3+} ions. The presence of more Ce^{3+} ions not only affects the lattice parameters but also influences the overall crystal structure and properties of the doped ceria materials. These structural changes have significant implications for the materials' oxygen storage capacity and crystallite size. The crystallite sizes of CeO_2 and doped CeO_2 were calculated using the equation[70,71] Γ (cm^{-1}) = 5 + 51.8/d (nm), where Γ represents the half width at half maximum (HWHM), and d is the crystallite size in nanometers for CeO_2 and Ni-doped CeO_2 samples. The crystallite size was determined to be 12.04 nm for pristine CeO_2, and 4.84 nm, 4.71 nm, and 4.50 nm for 1%, 5%, and 10% Ni-doped ceria, respectively. The difference in the crystallite sizes obtained from X-ray Diffraction (XRD) and Raman studies can be ascribed to the fundamental differences in the underlying principles of these techniques. The Scherrer analysis, based on X-ray diffraction (XRD), provides an estimate of the coherent diffraction domain size, which may be affected by factors such as lattice strain, instrumental broadening, and defects within the crystal structure. In contrast, Raman spectroscopy determines crystallite size through phonon confinement effects, which are more sensitive to local structural ordering and short-range interactions.

Furthermore, the broad band observed at 530–660 cm^{-1} in the Raman spectra confirms the highly disordered nature of doped CeO_2. To analyze the broad band range at 530–660 cm^{-1},

Table 1 Detailed values of the (111) peak position, FWHM, and crystallite size of CeO_2 and Ni-doped CeO_2

Materials	Peak position (2θ)	FWHM	Crystallite size (nm)
10% Ni/CeO_2	28.70	2.34	3.66
5% Ni/CeO_2	28.71	2.33	3.68
1% Ni/CeO_2	28.69	2.27	3.77
CeO_2	28.74	1.02	8.35

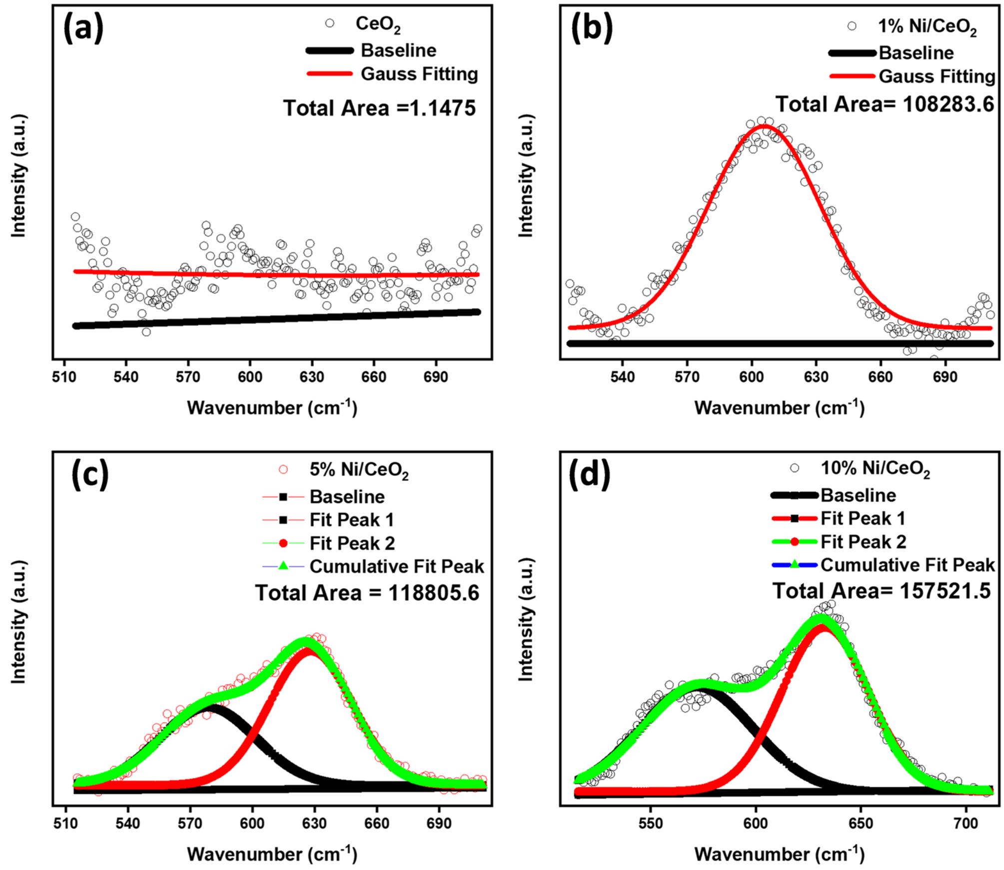

Fig. 2 Deconvolution of Raman spectra for (a) CeO$_2$ and (b), (c), and (d) for 1%, 5% and 10% Ni/CeO$_2$, respectively.

Table 2 Detailed values of the F$_{2g}$ peak position, HWMH, crystallite size, total area of the D band, and calculated ratio of $I_D/I_{F_{2g}}$ in Raman spectra for CeO$_2$ and Ni-doped CeO$_2$

Materials	Peak position (cm^{-1})	HWHM	Crystallite size (d) (nm)	Total area of the D band	$I_D/I_{F_{2g}}$
10% Ni/CeO$_2$	458	16.5	4.50	157 521.5	0.316
5% Ni/CeO$_2$	459	16.0	4.71	118 805.6	0.116
1% Ni/CeO$_2$	459.3	15.7	4.84	108 283.6	0.033
CeO$_2$	462	9.3	12.04	1.14	0.006

it was deconvoluted using a Gauss fitting, resulting in the calculated area under the band (Fig. 2). The area under the bands increased (Table 2) on increasing the concentration of Ni in CeO$_2$, which corresponds to the oxygen vacancies (Fig. 2). Moreover, an increase in the oxygen vacancies and lattice disorder ultimately leads to an increase in surface defects. Additionally, the observed ratio of the integrated area of the D band to that of the F$_{2g}$ peak ($I_D/I_{F_{2g}}$) serves as an indicator of the relative concentration of oxygen vacancies on the surface of doped CeO$_2$ and pristine CeO$_2$. A notable increase in the ($I_D/I_{F_{2g}}$) ratio is observed for the doped CeO$_2$, suggesting a higher density of oxygen vacancies compared to pristine CeO$_2$. The calculated $I_D/I_{F_{2g}}$ ratio is 0.006, 0.033, 0.116, and 0.316 for CeO$_2$ and 1%, 5% and 10% Ni/CeO$_2$, respectively, as illustrated in Table 2 and Fig. 2. This enhanced $I_D/I_{F_{2g}}$ ratio can be attributed to the strong interfacial interactions between Ni and CeO$_2$, which promote defect formation in doped ceria.

Furthermore, to ascertain the formation of oxygen vacancies in Ni-doped CeO$_2$ (Ni/CeO$_2$), the photoluminescence (PL) spectra of CeO$_2$ and Ni-doped CeO$_2$ (Ni/CeO$_2$) were measured in the wavelength range of 250–900 nm using an excitation wavelength of 532 nm, as shown in Fig. 3a. The PL emission intensities of pristine CeO$_2$ and Ni/CeO$_2$ display distinct trends, reiterating the doping of Ni in CeO$_2$. Compared to Ni/CeO$_2$, pristine CeO$_2$ exhibits higher PL intensity at a wavelength of 532 nm, corresponding to its larger bandgap energy (E_g = 3.31 eV). Furthermore, the PL intensity decreases with Ni doping in CeO$_2$. As the Ni concentration increases, the PL peak intensity decreases progressively, following the trend: CeO$_2$ > 1% Ni/CeO$_2$ > 5% Ni/CeO$_2$ > 10% Ni/CeO$_2$. This decline in PL intensity with increasing Ni doping can be attributed to the increase in defects, such as oxygen vacancies (Ce^{3+}), on the surface of CeO$_2$.[72,73] Notably, the 10% Ni/CeO$_2$ sample exhibits the lowest emission intensity, indicating a higher concentration of oxygen vacancies, which suggests that electron–hole recombination is effectively suppressed.[74] The suppression in electron–hole recombination is due to their efficient separation, which can be attributed to the interaction between Ni and CeO$_2$, resulting in the superior electrocatalytic efficiency of 10% Ni/CeO$_2$.[75]

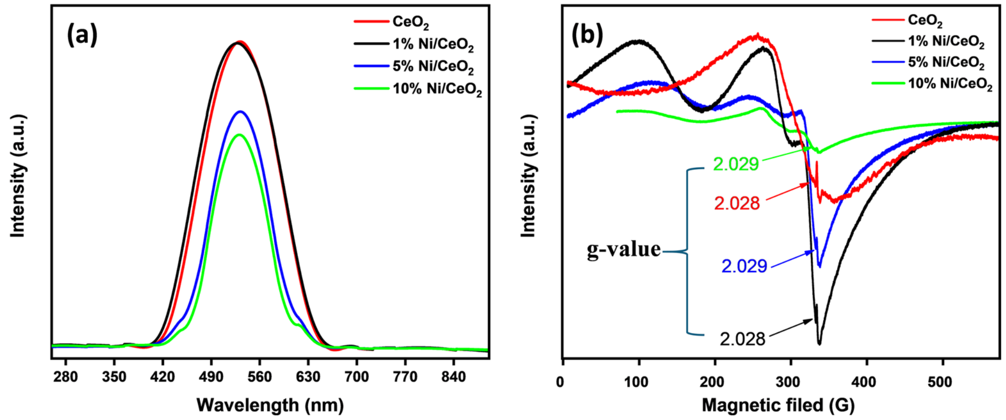

Fig. 3 PL (a) and EPR (b) spectra (inset calculated *g*-values) of CeO_2 and 1,5,10% Ni/CeO_2.

Electron paramagnetic resonance (EPR) is a non-invasive analytical method that examines the resonant energy absorption of electrons in materials when exposed to microwave electromagnetic radiation. Through EPR spectroscopy, the unpaired electrons within materials can be detected. Typically, unpaired electrons are localized at defects, dangling bonds, or dopant centers. So, to further ascertain the presence of defects in Ni-doped CeO_2 (Ni/CeO_2), electron paramagnetic resonance (EPR) analysis was conducted at room temperature for pristine CeO_2 and Ni/CeO_2 samples with varying nickel content (1%, 5%, and 10%) (Fig. 3b and Fig. S5, SI). Compared to pristine CeO_2, Ni/CeO_2 exhibited an EPR pattern with additional bands. The bands observed in the EPR spectra of CeO_2 and 1,5,10% Ni/CeO_2 at g values of 2.028, 2.028, 2.029 and 2.029, respectively, are attributed to the cubic sites of Ce^{3+} or physiosorbed oxygen molecules.[76] Additionally, the bands appearing at g values in the range 2.07–2.15 in Ni/CeO_2 are attributed to the O^{2-} species and Ce^{3+}–O^{-}–Ce^{4+} defect sites,[77] which are absent in pristine CeO_2 (Fig. S5, SI), confirming the enriched defects in Ni/CeO_2. Collectively, the findings from PXRD, Raman spectroscopy, XPS, PL and EPR analyses confirm the increase in oxygen vacancy defects on doping CeO_2 with Ni and the oxygen vacancy defects in the doped CeO_2 increase on increasing the dopant, Ni concentration.

3.2. Morphological analysis

3.2.1. FESEM and EDX analysis. To investigate the shapes and sizes, the synthesized Ni/CeO_2 was analyzed using a Field Emission Scanning Electron Microscope (FESEM). The FESEM image of Ni/CeO_2 depicted in Fig. 4a shows a spherical morphology. It is found that the material is composed of Ce, Ni and O in the desired amounts with no other impurities detected in the samples. The elemental mapping and chemical compositions of Ni/CeO_2 studied by EDX are shown in Fig. 4b and c. Fig. 4b shows that cerium (Ce), nickel (Ni) and oxygen (O) are uniformly distributed. The EDX spectrum shows the presence of 73.72% cerium, 3.72% nickel, and 22.56% oxygen, as detailed in the table (inset in Fig. 4c).

3.2.2. HRTEM analysis. To study the microstructure of Ni-doped CeO_2, High-Resolution Transmission Electron Microscopy (HRTEM) analysis was conducted. HRTEM images of pristine CeO_2 and Ni/CeO_2 particles are shown in Fig. 5a and Fig. S7a, SI. In the HRTEM image (Fig. 5b), the observed lattice fringe spacing of 0.312 nm corresponds to the (111) plane of CeO_2, confirming the presence of a well-defined crystalline structure. Notably, no distinct lattice fringes attributable to nickel were detected, suggesting that the prepared material exists in a single-phase structure without separate nickel crystallites, and this observation matches the result obtained from X-ray diffraction analysis, where no additional peak corresponding to Ni was observed. The selected area electron diffraction (SAED) pattern of Ni/CeO_2, shown in Fig. 5c, reveals a distinct ring pattern with bright dots. This pattern confirms the polycrystallinity of the synthesized nanomaterial. The *d*-values (interplanar spacings) for each ring from the large to the small ring in the SAED pattern for Ni/CeO_2 were calculated to verify the presence of cerium oxide. The calculated *d*-values, 0.311, 0.189, 0.156, and 0.123 nm, correspond to the crystal planes (111), (220), (222) and (331) of CeO_2, respectively. The *d*-spacing values closely align with those calculated from the X-ray diffraction (XRD) pattern of the CeO_2. The Ni/CeO_2 nanoparticles are estimated to be between 6–10 nm in size (Fig. S7b, SI), which is also in agreement with the values calculated from the X-ray diffraction (XRD) pattern.

3.3. X-ray photoelectron spectroscopy (XPS)

To evaluate the chemical composition, oxidation states and surface oxygen vacancies of the synthesized materials, X-ray photoelectron spectroscopic (XPS) analysis was carried out. In order to understand the effect of Ni on CeO_2, XPS spectra of Ni/CeO_2 were compared with those of pristine CeO_2. The XPS survey spectra of Ni/CeO_2 (Fig. 6a) confirm that the material consists of Ce, O, and Ni, with peaks in the binding energy ranges of 877–920 eV (Ce 3d), 527–535 eV (O 1s), and 840–890 eV (Ni 2p).[48,78] The high-resolution data were calibrated using the C 1s signal at 284.5 eV as a reference.[79] To investigate the oxidation states of Ce, the high-resolution Ce 3d core XPS spectra in the range from 877 to 920 eV were deconvoluted and fitted.

The eight peaks present in XPS spectra of Ce 3d, labeled as V, V′, V″, V‴, U, U′, U″ and U‴ correspond to the binding energies (eV) 916.6, 906.3, 903.3, 900.8, 898.3, 888.3, 885.2, and

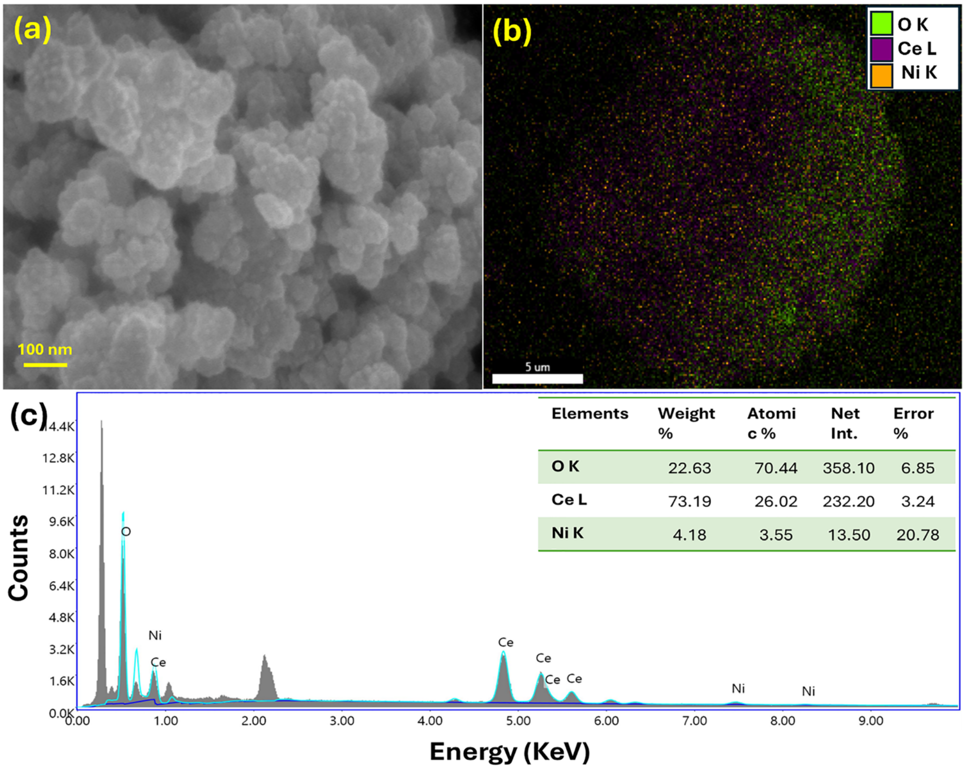

Elements	Weight %	Atomic %	Net Int.	Error %
O K	22.63	70.44	358.10	6.85
Ce L	73.19	26.02	232.20	3.24
Ni K	4.18	3.55	13.50	20.78

Fig. 4 (a) FESEM image, (b) overlay of O + Ce + Ni and (c) EDX spectra and corresponding chemical composition analysis of Ni/CeO_2.

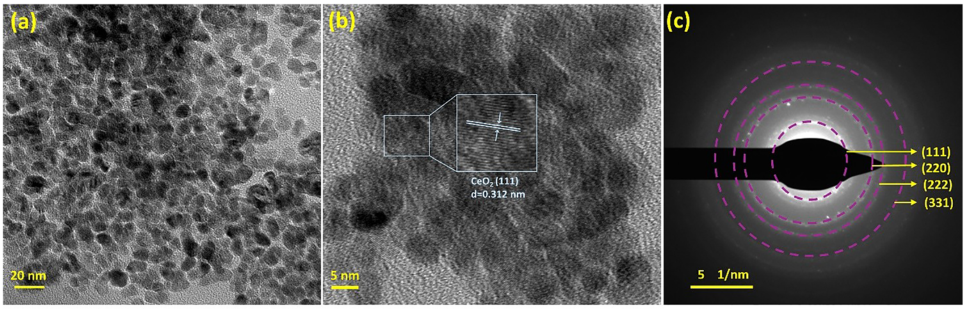

Fig. 5 (a) Low-resolution TEM image, (b) HRTEM image with the lattice fringes, and (c) the selected area electron diffraction (SAED) sequence of Ni/CeO_2.

882.3 shown in Fig. 6b. These binding energy values of Ce 3d agree with the previously reported studies.[80,81] Among them, two peaks appearing at 882.3 eV (U‴) and 903.3 eV (V″) correspond to Ce^{3+} $3d_{5/2}$ and Ce^{3+} $3d_{3/2}$, whereas the other peaks at 898.3 eV (U) and 916.6 eV (V) are attributed to the Ce^{4+} $3d_{5/2}$ and Ce^{4+} $3d_{3/2}$, respectively.[82] The presence of both Ce^{3+} and Ce^{4+} peaks in the Ce 3d spectra of CeO_2 confirms that these oxidation states coexist within the nanomaterial. The presence of Ce^{3+} and Ce^{4+} oxidation states causes the formation of defects, *i.e.*, oxygen vacancies in the CeO_2 lattice, due to the interconversion between Ce^{3+} and Ce^{4+}.

An oxygen vacancy is commonly associated with the loss or migration of oxygen atoms, which plays an important role in catalytic reactions.[83,84] The formation of oxygen vacancies on the surface of ceria is influenced by the dopant. It was observed that Ni doping changes the concentration of oxygen vacancies in ceria. In the Ni/CeO_2 composite, the Ce 3d XPS spectra reveal a noticeable decrease in the Ce^{4+} peak intensity along with a corresponding rise in Ce^{3+} peak intensity compared to pristine CeO_2 (Fig. S4a and b, SI). This rise in the Ce^{3+} peak intensity corresponds to an increase in oxygen vacancies in Ni/CeO_2, which can be attributed to the incorporation of Ni into the CeO_2 lattice. The proportion of Ce^{3+} can be quantified by calculating the ratio of the combined integrated areas of the Ce^{3+} peaks to the total integrated area of all peaks of Ce 3d in the form of the percentage of Ce^{3+} using the below eqn[85] and % of Ce^{3+} is shown in Table S1, SI.[86]

$$[Ce^{3+}] = \frac{(Ce^{3+})\text{Area}}{\sum(Ce^{4+} + Ce^{3+})\text{Area}} \times 100$$

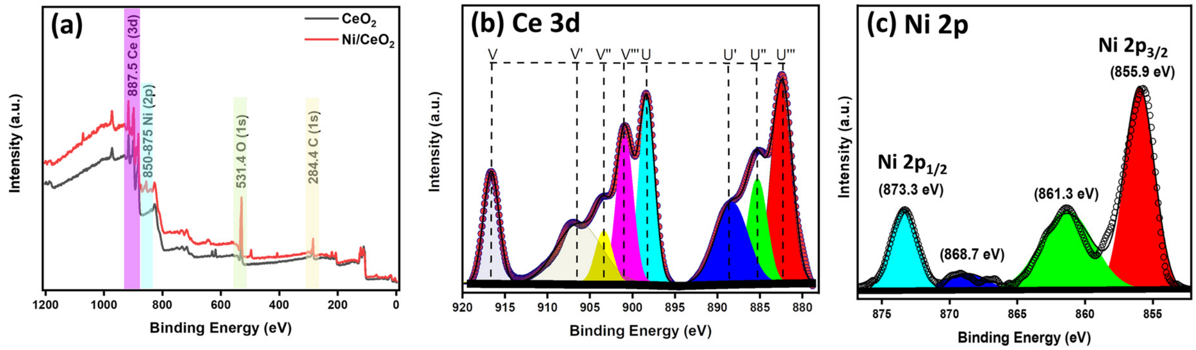

Fig. 6 The XPS survey of CeO_2 and Ni/CeO_2 (a), deconvoluted spectra of Ce 3d (b) and Ni 2p Ni/CeO_2 (c).

The Ce^{3+} content was found to be 25.17% and 14.39% for the Ni/CeO_2 and pristine CeO_2, respectively (Table S1, SI). The higher Ce^{3+} content in Ni/CeO_2 compared to pristine CeO_2 suggests higher oxygen vacancies in Ni/CeO_2, which can be attributed to the interfacial charge transfer between Ni and CeO_2. To further ascertain the extent of oxygen vacancies in Ni/CeO_2, the O 1s photoelectron spectra of Ni/CeO_2 and pristine CeO_2 (Fig. S4c and d, SI) were deconvoluted and compared. The main peaks around 529.9 eV and 532.1 eV (Fig. S4d, SI) correspond to lattice oxygen (O_L) (Ce^{+4}–O^{2-}) and oxygen vacancies (O_V) (Ce^{3+}–O^{2-}), respectively.[87] The intensities of the peak corresponding to oxygen vacancies are higher for Ni/CeO_2 compared to pristine CeO_2, which confirms the enhancement of oxygen vacancies in Ni/CeO_2. This result corroborates the observation from Ce 3d peaks and agrees with previous studies.[29,48] Additionally, the ratio of the area under the peaks (O_V/O_L) corresponding to oxygen, O 1s in CeO_2 and Ni/CeO_2 was determined to be 0.6 and 1.9, respectively, as shown in Table S2, SI. The higher O_V/O_L indicates a 3.1-fold increase in oxygen vacancies in Ni/CeO_2. Besides Ce, the presence of Ni is also ascertained from the peaks observed at 855.9 eV and 873.3 eV corresponding to Ni 2p$_{3/2}$ and Ni 2p$_{1/2}$, respectively, while the peaks at 861.3 eV and 868.7 eV represent the satellite peaks, as illustrated in Fig. 6c. These observed peaks for Ni match with the reported literature.[88,89]

3.4. Surface area measurement

To study the surface properties of the materials, such as surface area, pore diameter, and pore volume, the Brunauer–Emmett–Teller (BET) measurement was conducted. A nitrogen adsorption–desorption isotherm (Fig. 7a) was used to analyse the surface area and pore size distribution of pristine CeO_2 and Ni/CeO_2. From the isotherm, the porous feature of the materials is revealed from the steep increase in the curve at higher relative pressures. The pristine CeO_2 showed a surface area of 36.0 m^2 g^{-1}, a total pore volume of 0.15 cm^3 g^{-1}, and an average pore diameter of 7.5 nm. After the addition of Ni, the surface area increased to 39.9 m^2 g^{-1}, the pore volume increased to 0.21 cm^3 g^{-1}, and the pore diameter decreased to 5.4 nm. These changes in surface characteristics are attributed to the integration of Ni on CeO_2. The improved surface features facilitate the electrocatalytic activity in Ni/CeO_2.[90]

3.5. Thermal stability evaluation

Thermogravimetric analysis (TGA) was conducted between 30 °C and 800 °C at a heating rate of 10 °C min^{-1} to assess the thermal stability of both Ni/CeO_2 and pristine CeO_2. The thermograms (Fig. 7b) reveal two phases of weight loss. The first phase shows a rapid 21% weight loss between 30 °C and 283.3 °C, attributable to the removal of water molecules

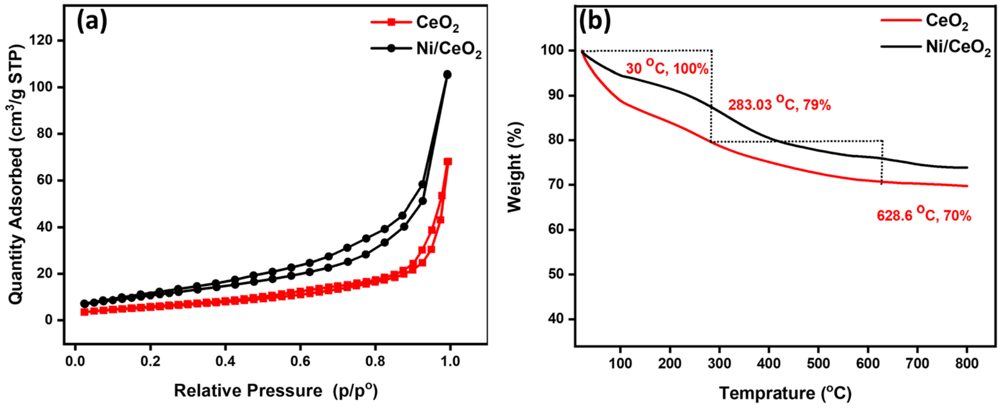

Fig. 7 (a) N_2 adsorption–desorption isotherms and (b) TGA analysis of CeO_2 and Ni/CeO_2.

physically adsorbed on the Ni/CeO_2 surface (Fig. 7b). The second phase exhibits a 9% weight loss between 283.03 °C and 628.6 °C, likely due to the thermal decomposition of residual nitrate species originating from precursor salts and possible interactions involving Ni and Ce ions.[91] After 628.03 °C, the Ni/CeO_2 catalyst shows minimal weight loss, indicating stability up to 800 °C. The weight losses were observed to be approximately 26% for Ni/CeO_2 and 30% for CeO_2. Notably, pristine CeO_2 loses more weight compared to the Ni/CeO_2, suggesting that the addition of Ni enhances the thermal stability of the electrocatalyst.

3.6. Oxygen evolution reaction (OER)

To evaluate the electrocatalytic performance of the materials and to understand the effect of incorporating Ni into CeO_2, electrodes of Ni-doped CeO_2 (Ni/CeO_2) and undoped CeO_2 were used in the oxygen evolution reaction (OER). The electrocatalytic performance for the OER of the electrodes, including (Nickel Foam) NF, NF/CeO_2, NF/1%Ni/CeO_2, NF/5%Ni/CeO_2, and NF/10% Ni/CeO_2, was investigated in a 1 M KOH solution using Ag/AgCl and Pt as the reference and counter electrodes, respectively. The linear sweep voltammogram for the OER performance of NF, NF/CeO_2, NF/1%Ni/CeO_2, NF/5%Ni/CeO_2, and NF/10%Ni/CeO_2 is shown in Fig. 8a. At a current density of 10 mA cm^{-2}, the overpotentials for NF, NF/CeO_2, NF/1%Ni/CeO_2, NF/5%Ni/CeO_2, and NF/10%Ni/CeO_2 were 442 mV, 406 mV, 384 mV, 357 mV, and 319 mV, respectively (as shown in Fig. 8b). There was a reduction in the overpotential when CeO_2 was incorporated in bare NF, confirming the catalytic role of CeO_2. The overpotential value was further reduced with Ni/CeO_2 compared to undoped CeO_2, indicating the effect of the dopant Ni. To understand the effect of the concentration of Ni, a varied amount of Ni was taken in Ni/CeO_2. Notably, the overpotential was further reduced with an increase in Ni content in Ni/CeO_2. There was a significant reduction in overpotential for the Ni/CeO_2 electrode with 10% Ni content compared to undoped CeO_2. Similarly, the current density was also influenced significantly by an increase in Ni content in Ni/CeO_2. Fig. 8c illustrates the current density for NF, NF/CeO_2, NF/1%Ni/CeO_2, NF/5%Ni/CeO_2, and NF/10%Ni/CeO_2 at an applied potential of 2.4 V *vs.* RHE. The corresponding values of the current densities were 78 mA cm^{-2}, 100 mA cm^{-2}, 104 mA cm^{-2}, 115 mA cm^{-2}, and 166 mA cm^{-2}, respectively (as shown in Fig. 8c). The values of overpotential and current density show enhanced OER activity for Ni/CeO_2 compared to undoped CeO_2. Incorporating CeO_2 onto NF enhanced the OER activity of NF/CeO_2 by reducing the overpotential by 36 mV and increasing the current density by 22 mA cm^{-2}. The OER activity was further improved by incorporating Ni into CeO_2. NF/1%Ni/CeO_2 exhibited an additional 22 mV reduction in overpotential and a 4 mA cm^{-2} increase in current density compared to NF/CeO_2. Interestingly, varying concentrations of Ni were also found to influence the electrocatalytic performance of the material. Further improvements were observed with increasing nickel content. NF/5%Ni/CeO_2 enhanced the OER performance, with a

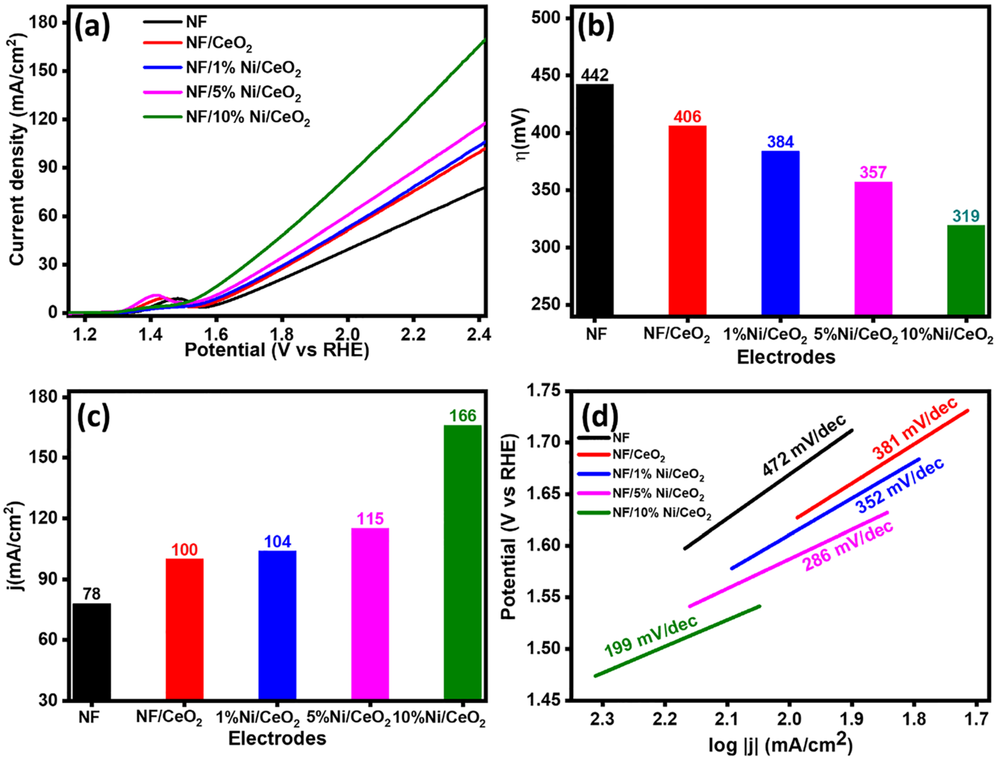

Fig. 8 (a) LSV curves, (b) overpotential (*vs.* RHE) at a current density of 10 mA cm^{-2}, (c) current density at a potential of 2.4 V, and (d) Tafel slope, for the OER for NF, NF/CeO_2, NF/1%Ni/CeO_2, NF/5%Ni/CeO_2, and NF/10%Ni/CeO_2.

Table 3 Summary of OER performance with electrocatalysts

Oxygen evolution reaction (OER)			
Electrocatalysts	Overpotential (mV) at 10 mA cm^{-2}	Current densities (mA cm^{-2})	Tafel slope (mV dec^{-1})
NF	442	78	472
NF/CeO_2	406	100	381
NF/1%Ni/CeO_2	384	104	352
NF/5%Ni/CeO_2	357	115	286
NF/10%Ni/CeO_2	319	166	199

reduction in the overpotential by 27 mV and an increase in the current density by 11 mA cm^{-2} compared to NF/1%Ni/CeO_2. The best performance was observed for NF/10%Ni/CeO_2, where the overpotential was significantly reduced by 38 mV, and the current density increased by 51 mA cm^{-2} compared to NF/5%Ni/CeO_2. Moreover, there was a remarkable decrease of 123 mV in the overpotential and a significant enhancement of 66 mA cm^{-2} in the current density for NF/10%Ni/CeO_2 compared to the NF/CeO_2 (undoped CeO_2). Fig. 8d represents the Tafel slopes for the OER for NF, NF/CeO_2, NF/1%Ni/CeO_2, NF/5%Ni/CeO_2, and NF/10%Ni/CeO_2, which were found to be 427 mV dec^{-1}, 381 mV dec^{-1}, 352 mV dec^{-1}, 286 mV dec^{-1} and 199 mV dec^{-1}, respectively, as shown in Table 3. The Tafel slope, an important kinetic parameter that determines the overpotential necessary to increase the current density, was significantly reduced by 48% in NF/10%Ni/CeO_2 compared to NF/CeO_2. The reaction mechanism for the OER can be given by the equations below:[92]

$$A + OH^- \rightleftharpoons A\text{–}OH + e^-$$

$$A\text{–}OH + OH^- \rightleftharpoons A\text{–}O + H_2O + e^-$$

$$A\text{–}O + OH^- \rightleftharpoons A\text{–}OOH + e^-/2A\text{–}O + OH^- \rightleftharpoons 2A + O_2 + 2e^-$$

$$A\text{–}OOH + OH^- \rightleftharpoons O_2 + H_2O + e^- + A$$

Here, A represents the active site.

3.7. Hydrogen evolution reaction (HER)

After investigating the OER performance, the electrocatalytic activity for the HER of the electrodes, including NF, NF/CeO_2, NF/1%Ni/CeO_2, NF/5%Ni/CeO_2, and NF/10%Ni/CeO_2, was also examined under the same experimental conditions. The LSV curves for the HER performance of NF, NF/CeO_2, NF/1%Ni/CeO_2, NF/5%Ni/CeO_2, and NF/10%Ni/CeO_2 are shown in Fig. 9a. The overpotentials calculated at a current density of 10 mA cm^{-2} for NF, NF/CeO_2, NF/1%Ni/CeO_2, NF/5%Ni/CeO_2, and NF/10%Ni/CeO_2, were 418 mV, 271 mV, 263 mV, 228 mV, and 212 mV, respectively, as shown in Fig. 9b. It was observed that there was a reduction in the overpotential with CeO_2 compared to bare NF proving the catalytic activity of CeO_2. The overpotential got further reduced with Ni/CeO_2, suggesting the improvement in catalytic activity on the introduction of dopant Ni in CeO_2. It's worth

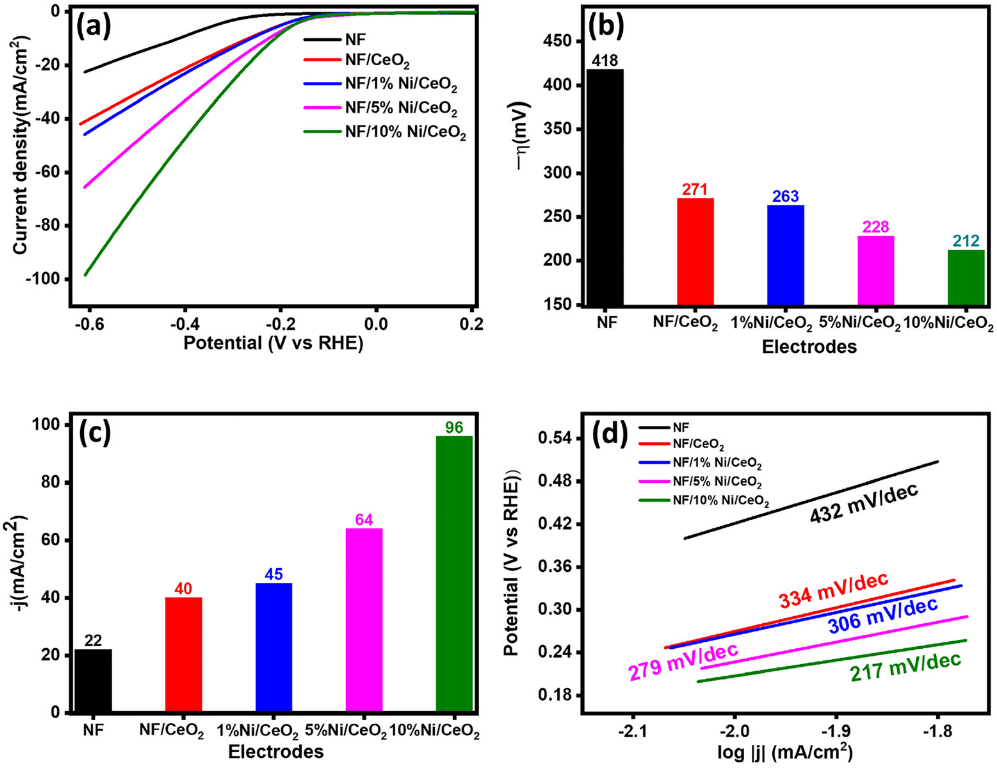

Fig. 9 (a) LSV curves, (b) overpotential (*vs.* RHE) at a current density of 10 mA cm^{-2}, (c) current density at a potential of −0.6 V, and (d) Tafel slope, for the HER for NF, NF/CeO_2, NF/1%Ni/CeO_2, NF/5%Ni/CeO_2, and NF/10%Ni/CeO_2.

noting that the overpotential got further reduced with Ni/CeO_2 on increasing Ni content. For NF/10%Ni/CeO_2, there was a significant reduction in the overpotential compared to undoped CeO_2. Similarly, the effect of Ni doping was found to be significant on the current density. Fig. 9c illustrates the current density at a potential of −0.6 V for NF, NF/CeO_2, NF/1%Ni/CeO_2, NF/5%Ni/CeO_2, and NF/10%Ni/CeO_2. The values of current density for NF, NF/CeO_2, NF/1%Ni/CeO_2, NF/5%Ni/CeO_2, and NF/10%Ni/CeO_2 were 22 mA cm^{-2}, 40 mA cm^{-2}, 45 mA cm^{-2}, 64 mA cm^{-2}, and 96 mA cm^{-2}, respectively (as shown in Fig. 9c). The current density increased with CeO_2 and the increase was more prominent with Ni/CeO_2 having 10% Ni content. The reduction in the overpotential and increase in the current density confirm the enhancement in the catalytic activity of the Ni/CeO_2 compared to undoped CeO_2. The highest HER performance was observed for NF/10%Ni/CeO_2, where the overpotential decreased by 59 mV, and the current density increased significantly by 56 mA cm^{-2} compared to undoped CeO_2. Fig. 9d represents the Tafel slope (HER) for NF, NF/CeO_2, NF/1%Ni/CeO_2, NF/5%Ni/CeO_2, and NF/10%Ni/CeO_2. The values of Tafel slopes for NF, NF/CeO_2, NF/1%Ni/CeO_2, NF/5%Ni/CeO_2, and NF/10%Ni/CeO_2 were found to be 432 mV dec^{-1}, 334 mV dec^{-1}, 306 mV dec^{-1}, 279 mV dec^{-1}, and 217 mV dec^{-1}, respectively, as shown in Table 4. The Tafel slope got reduced by 215 mV dec^{-1} for NF/10%Ni/CeO_2 compared to bare NF, indicating improved charge transfer kinetics in Ni/CeO_2. The best-performing electrode, NF/10%Ni/CeO_2, exhibited the lowest overpotentials (319 mV for the OER and 212 mV for the HER) and the highest current densities (166 mA cm^{-2} for the OER and 96 mA cm^{-2} for the HER). These results demonstrate that the incorporation of Ni in CeO_2 and increasing Ni content significantly enhance the electrocatalytic performance of the OER and HER. The reaction mechanism for the HER can be given by the equations below;[93]

$$A + H_2O + e^- \rightarrow A\text{–}H_{ad} + OH^-$$

$$2(A\text{–}H_{ad}) \rightarrow 2A + H_2$$

$$2(A\text{–}H_{ad}) + H_2O \rightarrow 2A + 2e^- + H_2 + H_2O$$

3.8. Electrochemical stability and gas evolution performance of Ni/CeO_2 electrodes

The electrochemical durability of the NF/10%Ni/CeO_2 electrode was evaluated through chronoamperometric analysis over a period of 6 hours. During this test, a constant potential of 1.48 V (*vs.* RHE) was maintained, and the variation in current density with time was continuously recorded. The corresponding chronoamperometric response (Fig. S6b, SI) reveals a stable current profile, indicating good operational stability of the electrode under prolonged anodic conditions.

Table 4 Summary of HER performance with the electrocatalysts

Hydrogen evolution reaction (HER)			
Electrocatalysts	Overpotential (mV) at 10 mA cm^{-2}	Current densities (mA cm^{-2})	Tafel slope (mV dec^{-1})
NF	418	22	432
NF/CeO_2	271	40	334
NF/1%Ni/CeO_2	263	45	306
NF/5%Ni/CeO_2	228	64	279
NF/10%Ni/CeO_2	212	96	217

Furthermore, to assess the stability of oxygen vacancies before and after the electrochemical measurements, Raman spectroscopy was carried out on the Ni/CeO_2 electrode (Fig. 10a). The electrode was fabricated *via* a drop-casting method using a catalyst (Ni/CeO_2), polyvinylidene fluoride (PVDF), and carbon black in a weight ratio of 85 : 10 : 5, respectively. The Raman spectrum of Ni/CeO_2 displays a strong peak at approximately 457 cm^{-1}, which corresponds to the F_{2g} vibrational mode, a signature feature of the fluorite crystal structure of ceria. In addition, a broad defect-related band is observed in the range of ∼560–660 cm^{-1}, which is commonly attributed to oxygen vacancy-induced lattice distortions in CeO_2. Importantly, post-electrocatalytic Raman analysis reveals that the intensity of this defect-associated band remains largely unchanged, with no noticeable decrease after the electrochemical study. This indicates that the oxygen vacancies are retained and are not significantly diminished during the electrocatalytic process. These observations demonstrate that the defect structure of ceria is robust with respect to electrocatalytic performance. In addition to the stability assessment, the evolution of hydrogen (H_2) and oxygen (O_2) gases was quantitatively examined for the Ni-doped CeO_2 (Ni/CeO_2) electrode using gas quantification techniques. These measurements were conducted at the respective onset potentials associated with the hydrogen evolution reaction (HER) and oxygen evolution reaction (OER). For OER evaluation, a potential of 1.48 V (*vs.* RHE) was applied, whereas HER measurements were performed at −0.6 V (*vs.* RHE). The amounts of H_2 and O_2 generated were monitored over time intervals of 100, 20, 40, and 60 minutes, as illustrated in Fig. 10b. The obtained results demonstrate that the Ni/CeO_2 electrode is capable of sustained gas evolution for both HER and OER processes. The consistent production of gases over time highlights the catalytic activity of the material, while also suggesting that Ni incorporation into the CeO_2 lattice plays a significant role in enhancing OER performance.

The Faradaic efficiency for hydrogen ($F.E._{H_2}$) and oxygen ($F.E._{O_2}$) was calculated using the following equations.[94]

$$FE_{H_2} = \frac{V_{\text{experiment}}}{V_{\text{theoretical}}} = \frac{V_{\text{experiment}}}{\left(\frac{2}{4}\right)\left(\frac{Q}{F}\right)V_{\text{m}}} \tag{1}$$

$$FE_{O_2} = \frac{V_{\text{experiment}}}{V_{\text{theoretical}}} \frac{V_{\text{experiment}}}{\left(\frac{2}{4}\right)\left(\frac{Q}{F}\right)V_{\text{m}}} \tag{2}$$

In these calculations, Q denotes the total charge, F is the Faraday constant, and V_{m} represents the molar volume of the gas.

The Ni/CeO_2 electrode exhibited high Faradaic efficiencies reaching up to 95.1% for hydrogen evolution and around 90% for oxygen evolution. These values indicate efficient charge utilization and demonstrate a promising electrochemical

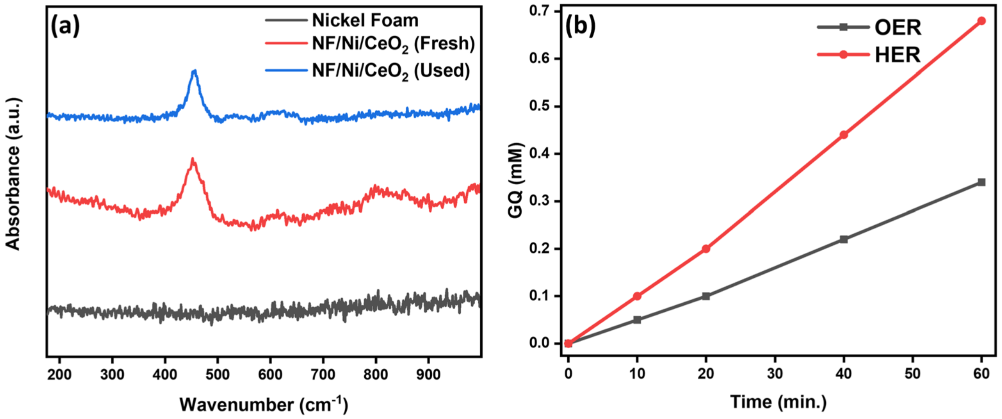

Fig. 10 (a) Comparison study of Raman spectra of nickel foam and Ni/CeO$_2$ electrodes recorded before and after electrocatalytic performance, highlighting the preservation of the characteristic defect-induced bands associated with oxygen vacancies and (b) evaluation of Faradaic efficiency for the Ni/CeO$_2$ electrode during the hydrogen evolution reaction (HER) and oxygen evolution reaction (OER).

performance of the electrode, with minimal energy losses during the conversion process.

4. Proposed mechanism for the OER and HER

Based on the results of structural characterization and the electrocatalysis experiments, the enhancement in OER performance for the Ni-doped CeO$_2$ electrode, NF/10%Ni/CeO$_2$, can be attributed to the increased concentration of oxygen vacancies due to the interaction of Ni and CeO$_2$. Ni doped in CeO$_2$ enhanced the oxygen vacancies, which are crucial in improving electrocatalytic performance (Fig. 11). A higher concentration of oxygen vacancies leads to an increase in active sites, thereby accelerating the OER process and reducing the required overpotential. Additionally, the incorporation of Ni induces the enhancement of spin-triplet O$_2$, which facilitates electron transfer by modulating the spin states, reducing spin-state energy barriers, and further improving the reaction kinetics. On the other hand, for NF/CeO$_2$ and NF/1%Ni/CeO$_2$, the enhancement in performance was relatively modest, as the lower Ni content resulted in fewer defects, *i.e.* oxygen vacancies. With only 1% Ni incorporation, the number of oxygen vacancies was not sufficient to induce a significant catalytic improvement, which is evident from the smaller reduction in overpotential and the slight increase in current density. A more pronounced reduction in overpotential was observed for Ni/CeO$_2$ compared to other previously reported CeO$_2$-based catalysts (Table 5). This observation is further supported by X-ray photoelectron spectroscopy (XPS) and other structural characterizations, which confirm that oxygen vacancy formation is more pronounced at higher Ni concentrations. Similarly, the enhanced HER performance observed for NF/10%Ni/CeO$_2$ can be attributed to the lower charge transfer resistance (R_{ct}), as confirmed by EIS measurements (Fig. S6a, SI). A lower R_{ct} signifies improved electron transport

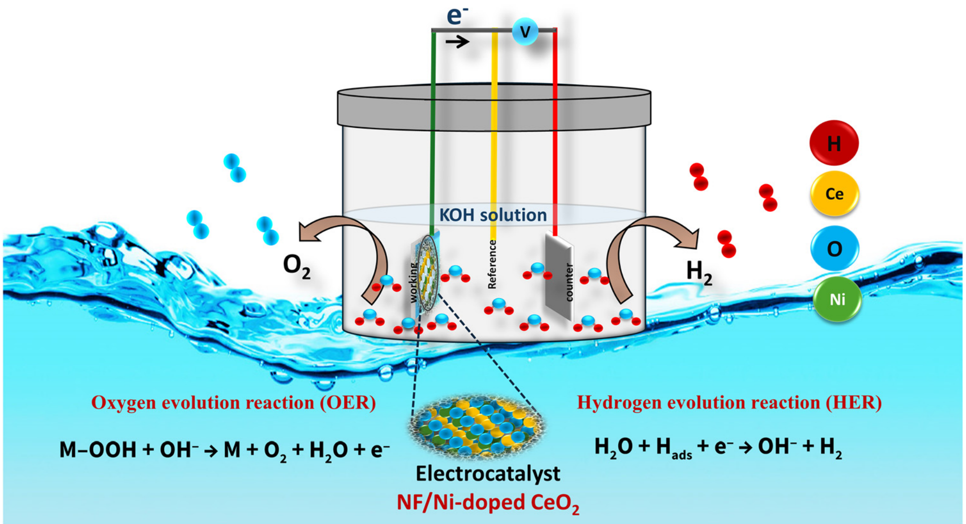

Fig. 11 Mechanism of electrocatalytic water splitting.

Table 5 Comparison of overpotential values for the HER and OER at a current density of 10 mA cm^{-2} in 1 M KOH solution, as reported in the literature, for different CeO_2-based catalysts

Electrocatalysts	Reaction	Overpotential (mV) @ 10 mA cm^{-2}	Ref.
Ni/Ceria	HER	588	95
Ni/Ceria-rGO	HER	208	52
CeO_2/Ni/NC	HER	320	96
NF/10%Ni/CeO_2	HER	212	This work
Ce–NiO–E	OER	382	97
(Ni–Fe–Co–Ce)O_x	OER	410	98
Ni–Ce/NC	OER	530	99
CeO_2/Ni/NC	OER	390	64
20%Ni + Fe-CeO_2	OER	380	100
NF/10% Ni/CeO_2	OER	319	This work

at the electrode–electrolyte interface, facilitating faster charge transfer and reducing the energy barrier for the HER process. The increased Ni content in CeO_2 enhances electrical conductivity and provides more active sites, which effectively reduces the impedance, allowing for efficient charge transport. This reduction in charge transfer resistance further justifies the significant decrease in overpotential and the increase in current density observed for NF/10%Ni/CeO_2.

5. Conclusions

In the quest for an efficient electrocatalyst, this study reports the design of ceria-based materials for the evolution of hydrogen and oxygen by electrocatalytic water splitting. While attaining significant improvement in electrocatalytic performance for nickel-doped ceria (Ni/CeO_2), it demonstrates how an increase in the concentration of the dopant increases oxygen vacancy defects in ceria, and an increase in defects in ceria enhances the electrocatalytic performance of Ni/CeO_2. We reported the preparation of Ni/CeO_2 that produced oxygen vacancy defects in ceria. Compared to pristine CeO_2, higher oxygen vacancies in Ni/CeO_2 confirmed the effect of the incorporation of Ni in CeO_2. Dopant concentration-dependent oxygen vacancy generation was ascertained. Generation of oxygen vacancies was verified by Raman spectroscopy, XPS, photoluminescence and EPR studies. Oxygen vacancies in Ni/CeO_2 were quantified by Raman spectroscopy studies. Detailed structural insights were derived from XRD, Raman, XPS, EDX, FESEM and HRTEM analysis. The stability of the catalysts was evaluated by TGA and chronoamperometry. Ni/CeO_2 was evaluated to be an effective electrocatalyst for the evolution of hydrogen and oxygen by water splitting, using linear sweep voltammetry. A significant reduction in overpotentials by 87 mV for oxygen evolution and 59 mV for hydrogen evolution was observed for Ni/CeO_2 compared to pristine CeO_2. Besides, there was a notable increase in current densities by 166 mA cm^{-2} for oxygen evolution and 96 mA cm^{-2} for hydrogen evolution. Also, faster reaction kinetics were observed from the reduction in the Tafel slope from 381 to 199 mV dec^{-1} for the OER and from 334 to 217 mV dec^{-1} for the HER. Electrochemical impedance spectroscopy (EIS) analysis revealed that the Ni/CeO_2 electrocatalyst exhibited the lowest charge transfer resistance, indicating enhanced interfacial charge transport and superior electrocatalytic activity. The electrocatalytic performance of Ni/CeO_2 was found to be affected by the increase in concentration of the dopant. Ni/CeO_2 with 10% nickel exhibited optimal performance, with substantial reductions in overpotential and a marked increase in current density with improved charge carrier dynamics. The enhanced electrocatalytic performance was attributed to the incorporation of Ni into ceria causing: (i) increased oxygen vacancy defects in Ni/CeO_2, (ii) enhancement of spin-triplet O_2, (iii) low charge transfer resistance (R_{ct}) facilitating electron transport at the electrode–electrolyte interface, (iv) enhancement in electrical conductivity and (v) reduction in impedance. This study concluded the synergistic interaction between Ni and CeO_2, defining the critical role of dopant concentration for modulating oxygen vacancies, which results in designing efficient water-splitting catalysts.

Conflicts of interest

The authors declare no competing financial interest.

Data availability

The data supporting this article have been included as part of the Supplementary Information (SI). Supplementary information: UV-vis absorption spectra, powder XRD peaks, Raman peak shift and intensity variation, XPS spectra of CeO_2, calculation of Ce^{3+} content from Ce 3d XPS spectra, oxygen vacancy calculation from O 1s in XPS spectra, O 1s XPS spectra, EPR spectra, electrocatalytic performance, and TEM image of CeO_2 and average particle size of Ni/CeO_2. See DOI: https://doi.org/10.1039/d6ma00528d.

Acknowledgements

NA acknowledges the grant Ref. No./IoE/2025-26/12/FRP under the Faculty Research Programme from the Institute of Eminence, University of Delhi. Ajit Kumar Dhanka thanks the Council of Scientific & Industrial Research (CSIR) and the University Grants Commission (UGC) for a Junior Research Fellowship (JRF)-16-6(119119 Dec. 2018/19). The authors would also like to acknowledge the University Science Instrumentation Centre (USIC) and Department of Physics & Astrophysics, University of Delhi, Special Centre for Nanoscience, Jawaharlal Nehru University (JNU), New Delhi, Central Research Facility (CRF), Indian Institute of Technology (IIT) Delhi, New Delhi, India, for the characterization facilities. The TEM facilities at the Sophisticated Analytical Instrumentation Facility (SAIF) at All India Institute of Medical Sciences (AIIMS), New Delhi, are gratefully acknowledged for the HRTEM measurements.

References

1 A. Hojjati-Najafabadi, R. Behmadi, Y. He, H. Kamyab and Y. Vasseghian, Tailoring high-entropy alloys for cutting-

edge hydrogen evolution electrocatalysis, *Sustainable Mater. Technol.*, 2025, e01655, DOI: 10.1016/j.susmat.2025.e01655.

2 J. Wang and W. Azam, Natural resource scarcity, fossil fuel energy consumption, and total greenhouse gas emissions in top emitting countries, *Geosci. Front.*, 2024, **15**(2), 101757, DOI: 10.1016/j.gsf.2023.101757.

3 S. Dale, *BP statistical review of world energy. BP Plc: London, UK, 14-16*, 2021, https://www.bp.com/content/dam/bp/business-sites/en/global/corporate/pdfs/energy-economics/statistical-review/bp-stats-review-2021-full-report.pdf.

4 F. A. Rosyid and T. Adachi, Coal mining in Indonesia: forecasting by the growth curve method: Rosyid FA, Adachi T, *Min. Econ.*, 2016, **29**(2), 71–85, DOI: 10.1007/s13563-016-0091-6.

5 M. Khaleel, Z. Yusupov, A. Ahmed, A. Alsharif, Y. Nassar and H. El-Khozondar, Towards sustainable renewable energy, *Appl. Sol. Energy*, 2023, **59**(4), 557–567, DOI: 10.3103/S0003701X23600704.

6 J. Wu, Y. He, R. Behmadi, N. Hojati, L. Xu, C. Li and A. Hojjati-Najafabadi, High-performance self-supporting FeCoNiCrMo HEA catalyst for alkaline hydrogen evolution, *J. Power Sources*, 2026, **669**, 239383, DOI: 10.1016/j.jpowsour.2026.239383.

7 L. Xu, S. Wu, X. He, H. Wang, D. Deng, J. Wu and H. Li, Interface engineering of anti-perovskite Ni3FeN/VN heterostructure for high-performance rechargeable zinc–air batteries, *Chem. Eng. J.*, 2022, **437**, 135291, DOI: 10.1016/j.cej.2022.135291.

8 P. Saha, F. A. Akash, S. M. Shovon, M. U. Monir, M. T. Ahmed, M. F. H. Khan and R. Akter, Grey, blue, and green hydrogen: A comprehensive review of production methods and prospects for zero-emission energy, *Int. J. Green Energy*, 2024, **21**(6), 1383–1397, DOI: 10.1080/15435075.2023.2244583.

9 L. Kaiwen, Y. Bin and Z. Tao, Economic analysis of hydrogen production from steam reforming process: A literature review, *Energy Sources, Part B*, 2018, **13**(2), 109–115, DOI: 10.1080/15567249.2017.1387619.

10 J. J. B. Caballero, I. N. Zaini and W. Yang, Reforming processes for syngas production: A mini-review on the current status, challenges, and prospects for biomass conversion to fuels, *Appl. Energy Combust. Sci.*, 2022, **10**, 100064, DOI: 10.1016/j.jaecs.2022.100064.

11 L. Chen, Z. Qi, S. Zhang, J. Su and G. A. Somorjai, Catalytic hydrogen production from methane: A review on recent progress and prospect, *Catalysts*, 2020, **10**(8), 858, DOI: 10.3390/catal10080858.

12 R. Kumar, R. Singh and S. Dutta, Review and outlook of hydrogen production through catalytic processes, *Energy Fuels*, 2024, **38**(4), 2601–2629, DOI: 10.1021/acs.energyfuels.3c04026.

13 A. Hojjati-Najafabadi, G. Heidari, M. Afsharpour, C. Belver, T. M. Aminabhavi, Y. Vasseghian and Y. He, Dual-functional hierarchical NiFe hydroxylphosphate electrocatalyst on copper dendrites for hydrogen and oxygen evolution, *Chem. Eng. J.*, 2025, **518**, 164622, DOI: 10.1016/j.cej.2025.164622.

14 J. X. Feng, S. H. Ye, H. Xu, Y. X. Tong and G. R. Li, Design and synthesis of FeOOH/CeO_2 heterolayered nanotube electrocatalysts for the oxygen evolution reaction, *Adv. Mater.*, 2016, **28**(23), 4698–4703, DOI: 10.1002/adma.201600054.

15 T. Li, S. Li, Q. Liu, Y. Tian, Y. Zhang, G. Fu and Y. Tang, Hollow Co_3O_4/CeO_2 heterostructures in situ embedded in N-doped carbon nanofibers enable outstanding oxygen evolution, *ACS Sustainable Chem. Eng.*, 2019, **7**(21), 17950–17957, DOI: 10.1021/acssuschemeng.9b04699.

16 Y. He, R. Tan, L. Li, R. Behmadi, S. Sun, C. Zhu and A. Hojjati-Najafabadi, Electrospinning-Derived FeCrNiZrMn High-Entropy Alloy on Carbon Nanofibers for Hydrogen Evolution, *ChemCatChem*, 2026, **18**(3), e01811, DOI: 10.1002/cctc.202501811.

17 X. Li, Z. Wang and L. Wang, Metal–organic framework-based materials for solar water splitting, *Small Sci.*, 2021, **1**(5), 2000074, DOI: 10.1002/smsc.202000074.

18 K. Mishra, N. Devi, S. S. Siwal, V. K. Gupta and V. K. Thakur, Hybrid semiconductor photocatalyst nanomaterials for energy and environmental applications: fundamentals, designing, and prospects, *Adv. Sustainable Syst.*, 2023, **7**(8), 2300095, DOI: 10.1002/adsu.202300095.

19 S. Li, X. Zhang, F. Yang, J. Zhang, W. Shi and F. Rosei, Mechanically driven water splitting over piezoelectric nanomaterials, *Chem. Catal.*, 2024, **4**(2), 100901, DOI: 10.1016/j.checat.2024.100901.

20 G. A. Tigwere, M. D. Khan, L. D. Nyamen, F. M. de Souza, W. Lin, R. K. Gupta and P. T. Ndifon, Transition metal (Ni, Cu and Fe) doped MnS nanostructures: effect of doping on supercapacitance and water splitting, *Mater. Sci. Semicond. Process.*, 2023, **158**, 107365, DOI: 10.1016/j.mssp.2023.107365.

21 D. Liu and Y. Kuang, The borophene quantum dots scaffolded TiO_2 nanocomposite as an efficient photo electrocatalyst for water splitting application, *Appl. Surf. Sci.*, 2024, **646**, 158910, DOI: 10.1016/j.apsusc.2023.158910.

22 A. Mehtab, S. M. Alshehri and T. Ahmad, Photocatalytic and photoelectrocatalytic water splitting by porous g-C_3N_4 nanosheets for hydrogen generation, *ACS Appl. Nano Mater.*, 2022, **5**(9), 12656–12665, DOI: 10.1021/acsanm.2c02460.

23 H. Mohan and T. Shin, Enhanced photocatalytic water-splitting performance of Fe/CdS nanomaterials: Structural, optical, and electrochemical insights, *Mater. Sci. Semicond. Process.*, 2025, **199**, 109892, DOI: 10.1016/j.mssp.2025.109892.

24 D. J. Li, Z. G. Gu, W. Zhang, Y. Kang and J. Zhang, Epitaxial encapsulation of homodispersed CeO_2 in a cobalt–porphyrin network derived thin film for the highly efficient oxygen evolution reaction, *J. Mater. Chem. A*, 2017, **5**(38), 20126–20130, DOI: 10.1039/C7TA06580A.

25 A. Sivanantham, P. Ganesan and S. Shanmugam, A synergistic effect of Co and CeO_2 in nitrogen-doped carbon nanostructure for the enhanced oxygen electrode activity and stability, *Appl. Catal., B*, 2018, **237**, 1148–1159, DOI: 10.1016/j.apcatb.2017.08.063.

26 K. Ghemit, F. Z. Akika, K. Rouibah, M. Benamira, D. Bousba, A. Gouasmia and I. Avramova, Photocatalytic activity of the new $NiAl_2O_4/CeO_2$ heterojunction for the elimination of Rose Bengal under solar irradiation, *Inorg. Chem. Commun.*, 2025, **176**, 114185, DOI: 10.1016/j.inoche.2025.114185.

27 A. Krishnan, K. Archana, A. S. Arsha, A. Viswam and M. S. Meera, Divulging the potential role of wide band gap semiconductors in electro and photo catalytic water splitting for green hydrogen production, *Chin. J. Catal.*, 2025, **68**, 103–154, DOI: 10.1016/S1872-2067(24)60156-7.

28 J. Mazloom, F. E. Ghodsi, F. Z. Tepehan, G. G. Tepehan and I. Turhan, Enhanced lithium electrochemical performance and optical properties of CeO_2–SnO_2 nanocomposite thin films by transition metal (TM: Ni, Mn, and Co) doping, *J. Sol–Gel Sci. Technol.*, 2018, **86**, 51–62, DOI: 10.1007/s10971-018-4603-4.

29 N. V. Bôas, J. B. S. Junior, L. C. Varanda, S. A. S. Machado and M. L. Calegaro, Bismuth and cerium doped cryptomelane-type manganese dioxide nanorods as bifunctional catalysts for rechargeable alkaline metal-air batteries, *Appl. Catal., B*, 2019, **258**, 118014, DOI: 10.1016/j.apcatb.2019.118014.

30 S. Dai, E. Montero-Lanzuela, A. Tissot, H. G. Baldoví, H. García, S. Navalón and C. Serre, Room temperature design of Ce (IV)-MOFs: from photocatalytic HER and OER to overall water splitting under simulated sunlight irradiation, *Chem. Sci.*, 2023, **14**(13), 3451–3461, DOI: 10.1039/D2SC05161C.

31 S. Ghosh, S. Pal, M. Biswas, M. Thandavarayan, A. A. Reddy and M. K. Naskar, Dual Active Site Mediated Photocatalytic H_2 Evolution through Water Splitting Using CeO_2/PPy/BFO Double Heterojunction Catalyst, *ACS Appl. Energy Mater.*, 2024, **7**(24), 11453–11465, DOI: 10.1021/acsaem.4c00269.

32 A. K. Dhanka, M. Tiwari, P. K. Bhartiya, B. Pani, N. Agasti and D. Mishra, Oxygen vacancies induced low overpotentials of Ag/CeO_2 for electrocatalytic evolution of oxygen and hydrogen, *Mater. Adv.*, 2025, **6**(11), 3716–3729, DOI: 10.1039/D5MA00321K.

33 G. Liu, M. Wang, Y. Wu, N. Li, F. Zhao, Q. Zhao and J. Li, 3D porous network heterostructure NiCe@NiFe electrocatalyst for efficient oxygen evolution reaction at large current densities, *Appl. Catal., B*, 2020, **260**, 118199, DOI: 10.1016/j.apcatb.2019.118199.

34 J. Song, C. Wei, Z. F. Huang, C. Liu, L. Zeng, X. Wang and Z. J. Xu, A review on fundamentals for designing oxygen evolution electrocatalysts, *Chem. Soc. Rev.*, 2020, **49**(7), 2196–2214, DOI: 10.1039/C9CS00607A.

35 E. Demir, S. Akbayrak, A. M. Önal and S. Özkar, Ceria supported ruthenium(0) nanoparticles: Highly efficient catalysts in oxygen evolution reaction, *J. Colloid Interface Sci.*, 2019, **534**, 704–710, DOI: 10.1016/j.jcis.2018.09.07.

36 S. Jiang, R. Zhang, H. Liu, Y. Rao, Y. Yu, S. Chen and Y. Kang, Promoting formation of oxygen vacancies in two-dimensional cobalt-doped ceria nanosheets for efficient hydrogen evolution, *J. Am. Chem. Soc.*, 2020, **142**(14), 6461–6466, DOI: 10.1021/jacs.9b13915.

37 Y. He, J. Wu, F. Hu, L. Mao, T. M. Aminabhavi, Y. Vasseghian and A. Hojjati-Najafabadi, Self-supporting FeCoNiCuTiGa high-entropy alloy electrodes for alkaline hydrogen and oxygen evolution reactions: experimental and theoretical insights, *ACS Appl. Energy Mater.*, 2024, **7**(20), 9121–9133, DOI: 10.1021/acsaem.4c01036.

38 S. Selvanathan, P. M. Woi and R. Srivastava, Transition metal-based single-atom catalyst for photoelectrochemical water splitting, in *Solar-Driven Green Hydrogen Generation and Storage*, Elsevier, 2023, pp. 61–85, DOI: 10.1016/B978-0-323-99580-1.00001-7.

39 Z. Yang, D. Zheng, X. Yue, K. Wang, Y. Hou, W. Dai and X. Fu, The synergy of Ni doping and oxygen vacancies over CeO_2 in visible light-assisted thermal catalytic methanation reaction, *Appl. Surf. Sci.*, 2023, **615**, 156311, DOI: 10.1016/j.apsusc.2022.156311.

40 P. K. Mishra, S. Acharya, A. Palai, S. K. Sahu, A. Meher and D. Sahu, Strategic Ni integration to study its impact on the photoluminescence and photocatalytic performances of SnO_2 nanorod architecture, *Chem. Inorg. Mater.*, 2024, **3**, 100055, DOI: 10.1016/j.cinorg.2024.100055.

41 Y. Zhang, P. Guo, S. Li, J. Sun, W. Wang, B. Song and P. Xu, Magnetic field assisted electrocatalytic oxygen evolution reaction of nickel-based materials, *J. Mater. Chem. A*, 2022, **10**(4), 1760–1767, DOI: 10.1039/D1TA09444K.

42 T. Sun, Z. Tang, W. Zang, Z. Li, J. Li, Z. Li and J. Lu, Ferromagnetic single-atom spin catalyst for boosting water splitting, *Nat. Nanotechnol.*, 2023, **18**(7), 763–771, DOI: 10.1038/s41565-023-01407-1.

43 M. Tiwari and D. Mishra, Enhanced spin-polarization and detection limit in a spin-based optoelectrochemical DNA hybridization sensor induced by circularly polarized light, *Sens. Diagn.*, 2024, **3**(7), 1159–1166, DOI: 10.1039/D4SD00109E.

44 F. A. C. Oliveira, M. A. Barreiros, A. Haeussler, A. P. Caetano, A. I. Mouquinho, P. M. O. e Silva and S. Abanades, High performance cork-templated ceria for solar thermochemical hydrogen production *via* two-step water-splitting cycles, *Sustainable Energy Fuels*, 2020, **4**(6), 3077–3089, DOI: 10.1039/D0SE00318B.

45 P. A. Koyale, S. V. Mulik, J. L. Gunjakar, T. D. Dongale, V. B. Koli, N. B. Mullani and S. D. Delekar, Synergistic enhancement of water-splitting performance using mof-derived ceria-modified g-C_3N_4 nanocomposites: Synthesis, performance evaluation, and stability prediction with machine learning, *Langmuir*, 2024, **40**(26), 13657–13668, DOI: 10.1021/acs.langmuir.4c01336.

46 M. Orfila, D. Sanz, M. Linares, R. Molina, R. Sanz, J. Marugán and J. Á. Botas, H2 production by thermochemical water splitting with reticulated porous structures of ceria-based mixed oxide materials, *Int. J. Hydrogen Energy*, 2021, **46**(33), 17458–17471, DOI: 10.1016/j.ijhydene.2020.04.222.

47 K. Yan, C. Wen, R. Li, B. Zhang, T. Liu, Q. Liu and Z. Zhou, Morphological optimized CeO_2 and Cu-doped CeO_2 nanocrystals for hydrogen production by solar photo-thermochemical water splitting based on surface photoinduced oxygen

vacancies, *Appl. Surf. Sci.*, 2023, **636**, 157779, DOI: 10.1016/j.apsusc.2023.157779.

48 A. Haghighatzadeh, Enhanced third-order optical susceptibility in Ag-doped CeO_2 nanostructures under pulsed Nd-YVO_4 laser, *Opt. Laser Technol.*, 2020, **126**, 106114, DOI: 10.1016/j.optlastec.2020.106114.

49 M. Tiwari, P. K. Bhartiya, N. Bangruwa, S. K. Sarkar and D. Mishra, Spin Polarization and Phase Transformation-Aided Efficient Overall Water Splitting Using $Ni_{50}Mn_{18}Ga_{25}Cu_7$ Ferromagnetic Shape Memory Heusler Alloy, *ACS Appl. Mater. Interfaces*, 2024, **16**(50), 69398–69409, DOI: 10.1021/acsami.4c15932.

50 S. Sagadevan, M. R. Johan and J. A. Lett, Fabrication of reduced graphene oxide/CeO_2 nanocomposite for enhanced electrochemical performance, *Appl. Phys.*, 2019, **125**(315), 1–11, DOI: 10.1007/s00339-019-2625-6.

51 S. Sagadevan, M. R. Johan and J. A. Lett, Fabrication of reduced graphene oxide/CeO_2 nanocomposite for enhanced electrochemical performance, *Appl. Phys. A*, 2019, **125**(5), 315, DOI: 10.1007/s00339-019-2625-6.

52 S. Yousefali, A. Reyhani, S. Z. Mortazavi, N. Yousefali and A. Rajabpour, UV-blue spectral down-shifting of titanium dioxide nano-structures doped with nitrogen on the glass substrate to study its anti-bacterial properties on the E. coli bacteria, *Surf. Interfaces*, 2018, **13**, 11–21, DOI: 10.1016/j.surfin.2018.07.003.

53 A. K. Dhanka, E. C. Kohlrausch, R. Samantray, V. Kumar, B. Pani and N. Agasti, Harnessing defects in Ag/CeO_2 for enhanced photocatalytic degradation of antibiotic in water: Structural characteristics, in-depth insights on mechanism, degradation pathway, *Chem. Eng. J. Adv.*, 2025, **21**, 100706, DOI: 10.1016/j.ceja.2025.100706.

54 S. Selvaraj, M. K. Mohan, M. Navaneethan, S. Ponnusamy and C. Muthamizhchelvan, Synthesis and photocatalytic activity of Gd doped ZnO nanoparticles for enhanced degradation of methylene blue under visible light, *Mater. Sci. Semicond. Process.*, 2019, **103**, 104622, DOI: 10.1016/j.mssp.2019.104622.

55 J. Saranya, K. S. Ranjith, P. Saravanan, D. Mangalaraj and R. T. R. Kumar, Cobalt-doped cerium oxide nanoparticles: enhanced photocatalytic activity under UV and visible light irradiation, *Mater. Sci. Semicond. Process.*, 2014, **26**, 218–224, DOI: 10.1016/j.mssp.2014.03.054.

56 F. Su, P. Li, J. Huang, M. Gu, Z. Liu and Y. Xu, Photocatalytic degradation of organic dye and tetracycline by ternary Ag_2O/AgBr–CeO_2 photocatalyst under visible-light irradiation, *Sci. Rep.*, 2021, **11**(1), 85, DOI: 10.1038/s41598-020-76997-0.

57 A. K. Dhanka, B. Pani and N. Agasti, Defect-enriched CuO/CeO_2 nanostructure: in-depth structural characterization and photocatalytic performance, *RSC Adv.*, 2025, **15**(15), 11774–11789, DOI: 10.1039/D5RA00640F.

58 M. Kazazi, B. Moradi and M. Delshad Chermahini, Enhanced photocatalytic degradation of methyl orange using Ag/Sn-doped CeO_2 nanocomposite, *J. Mater. Sci.: Mater. Electron.*, 2019, **30**, 6116–6126, DOI: 10.1007/s10854-019-00913-0.

59 S. Kumar and A. K. Ojha, Ni, Co and Ni–Co codoping induced modification in shape, optical band gap and enhanced photocatalytic activity of CeO_2 nanostructures for photodegradation of methylene blue dye under visible light irradiation, *RSC Adv.*, 2016, **6**(11), 8651–8660, DOI: 10.1039/C5RA14184B.

60 P. Tamizhdurai, S. Sakthinathan, S. M. Chen, K. Shanthi, S. Sivasanker and P. Sangeetha, Environmentally friendly synthesis of CeO_2 nanoparticles for the catalytic oxidation of benzyl alcohol to benzaldehyde and selective detection of nitrite, *Sci. Rep.*, 2017, **7**(1), 46372, DOI: 10.1038/srep46372.

61 G. Jayakumar, A. A. Irudayaraj, A. D. Raj, S. J. Sundaram and K. Kaviyarasu, Electrical and magnetic properties of nanostructured Ni doped CeO_2 for optoelectronic applications, *J. Phys. Chem. Solids*, 2022, **160**, 110369, DOI: 10.1016/j.jpcs.2021.110369.

62 S. Muduli and T. R. Sahoo, Green synthesis and characterization of CeO_2 and Ni-doped CeO_2 nanoparticles and its dielectric properties, *Mater. Today: Proc.*, 2023, **74**, 697–702, DOI: 10.1016/j.matpr.2022.10.278.

63 N. Mahmoudi Khatir, Z. Abdul-Malek, A. K. Zak, A. Akbari and F. Sabbagh, Sol–gel grown Fe-doped ZnO nanoparticles: antibacterial and structural behaviors, *J. Sol–Gel Sci. Technol.*, 2016, **78**(1), 91–98, DOI: 10.1007/s10971-015-3922-y.

64 S. Mustapha, M. M. Ndamitso, A. S. Abdulkareem, J. O. Tijani, D. T. Shuaib, A. K. Mohammed and A. Sumaila, Comparative study of crystallite size using Williamson-Hall and Debye-Scherrer plots for ZnO nanoparticles, *Adv. Nat. Sci.: Nanosci. Nanotechnol.*, 2019, **10**(4), 045013, DOI: 10.1088/2043-6254/ab52f7.

65 Y. Ren, Q. Jiang, J. Yang, Y. Luo, D. Zhang, Y. Cheng and Z. Zhou, Enhanced thermoelectric performance of MnTe via Cu doping with optimized carrier concentration, *J. Materiomics*, 2016, **2**(2), 172–178, DOI: 10.1016/j.jmat.2016.05.008.

66 S. Jafari and Z. Shaghaghi, CeO_2/CuO/NiO hybrid nanostructures loaded on N-doped reduced graphene oxide nanosheets as an efficient electrocatalyst for water oxidation and non-enzymatic glucose detection, *Dalton Trans.*, 2023, **52**(22), 7564–7580, DOI: 10.1039/D3DT00527E.

67 J. Zimou, K. Nouneh, R. Hsissou, A. El-Habib, L. El Gana, A. Talbi and M. Addou, Structural, morphological, optical, and electrochemical properties of Co-doped CeO_2 thin films, *Mater. Sci. Semicond. Process.*, 2021, **135**, 106049, DOI: 10.1016/j.mssp.2021.106049.

68 N. Kainbayev, M. Sriubas, D. Virbukas, Z. Rutkuniene, K. Bockute, S. Bolegenova and G. Laukaitis, Raman study of nanocrystalline-doped ceria oxide thin films, *Coatings*, 2020, **10**(5), 432, DOI: 10.3390/coatings10050432.

69 Y. Xu, C. F. Miller and L. L. Claiborne, Estimating Ce^{4+} and Ce^{3+} concentrations in zircon and coexisting melts, with implications for constraining oxygen fugacity, *Chem. Geol.*, 2024, **663**, 122283, DOI: 10.1016/j.chemgeo.2024.122283.

70 B. Vigneshwaran, P. Kuppusami, S. Ajithkumar and M. Kuppusamy, Temperature-dependent Raman and

dielectric studies of Sm and Zr Co-doped $BaTiO_3$ ceramics, *J. Mater. Sci.: Mater. Electron.*, 2024, **35**(5), 353, DOI: 10.1007/s10854-024-12060-2.

71 S. S. Negi, H. M. Kim, B. S. Cheon, C. H. Jeong, H. S. Roh and D. W. Jeong, Restructuring Co–CoOx Interface with Titration Rate in Co/Nb-CeO_2 Catalysts for Higher Water–Gas Shift Performance, *ACS Appl. Mater. Interfaces*, 2023, **15**(44), 51013–51024, DOI: 10.1021/acsami.3c09312.

72 G. Murugadoss, T. Kannappan, J. R. Rajabathar, R. K. Manavalan, S. T. Salammal and N. Venkatesh, Rapid photocatalytic activity of crystalline CeO_2-CuO-$Cu(OH)_2$ ternary nanocomposite, *Sustainability*, 2023, **15**(21), 15601, DOI: 10.3390/su152115601.

73 S. Tiwari, G. Rathore, N. Patra, A. K. Yadav, D. Bhattacharya, S. N. Jha and S. Sen, Oxygen and cerium defects mediated changes in structural, optical and photoluminescence properties of Ni substituted CeO_2, *J. Alloys Compd.*, 2019, **782**, 689–698, DOI: 10.1016/j.jallcom.2018.12.009.

74 X. J. Wen, C. G. Niu, L. Zhang, C. Liang and G. M. Zeng, A novel Ag_2O/CeO_2 heterojunction photocatalysts for photocatalytic degradation of enrofloxacin: possible degradation pathways, mineralization activity and an in depth mechanism insight, *Appl. Catal., B*, 2018, **221**, 701–714, DOI: 10.1016/j.apcatb.2017.09.060.

75 K. Zhang, S. Lv, Z. Lin and D. Tang, CdS: Mn quantum dot-functionalized g-C3N4 nanohybrids as signal-generation tags for photoelectrochemical immunoassay of prostate specific antigen coupling DNAzyme concatamer with enzymatic biocatalytic precipitation, *Biosens. Bioelectron.*, 2017, **95**, 34–40, DOI: 10.1016/j.bios.2017.04.005.

76 M. Wang, M. Shen, X. Jin, J. Tian, Y. Shao, L. Zhang and J. Shi, Exploring the enhancement effects of hetero-metal doping in CeO_2 on CO_2 photocatalytic reduction performance, *Chem. Eng. J.*, 2022, **427**, 130987, DOI: 10.1016/j.cej.2021.130987.

77 L. Wang, Y. Yu, H. He, Y. Zhang, X. Qin and B. Wang, Oxygen vacancy clusters essential for the catalytic activity of CeO_2 nanocubes for o-xylene oxidation, *Sci. Rep.*, 2017, **7**(1), 1–11, DOI: 10.1038/s41598-017-13178-6.

78 R. Murugan, G. Ravi, G. Vijayaprasath, S. Rajendran, M. Thaiyan, M. Nallappan and Y. Hayakawa, Ni–CeO_2 spherical nanostructures for magnetic and electrochemical supercapacitor applications, *Phys. Chem. Chem. Phys.*, 2017, **19**(6), 4396–4404, DOI: 10.1039/C6CP08281E.

79 I. K. Sideri, R. Arenal and N. Tagmatarchis, Terpyridine-functionalized single-walled carbon nanotubes towards selectivity in the oxygen reduction reaction, *Nanoscale Adv.*, 2025, **7**(14), 4469–4479, DOI: 10.1039/D5NA00281H.

80 S. K. Alla, P. Kollu, S. S. Meena, H. K. Poswal, C. L. Prajapat, R. K. Mandal and N. K. Prasad, Investigation of magnetic properties for Hf^{4+} substituted CeO_2 nanoparticles for spintronic applications, *J. Mater. Sci.: Mater. Electron.*, 2018, **29**(12), 10614–10623, DOI: 10.1007/s10854-018-9125-x.

81 S. Zuo, Y. He, Y. You, X. Shu, M. Wen, Y. Lu and X. Lu, Free occupying mechanism of simulated tetravalent waste ions in $Gd_2Zr_2O_7$ and performance evaluation of the waste forms, *J. Am. Ceram. Soc.*, 2023, **106**(11), 7088–7097, DOI: 10.1111/jace.19303.

82 R. Bortamuly, G. Konwar, P. K. Boruah, M. R. Das, D. Mahanta and P. Saikia, CeO_2-PANI-HCl and CeO_2-PANI-PTSA composites: synthesis, characterization, and utilization as supercapacitor electrode materials, *Ionics*, 2020, **26**(11), 5747–5756, DOI: 10.1007/s11581-020-03690-7.

83 Y. Zheng, K. Fu, Z. Yu, Y. Su, R. Han and Q. Liu, Oxygen vacancies in a catalyst for VOCs oxidation: synthesis, characterization, and catalytic effects, *J. Mater. Chem. A*, 2022, **10**(27), 14171–14186, DOI: 10.1039/D2TA03180A.

84 K. Yu, L. L. Lou, S. Liu and W. Zhou, Asymmetric oxygen vacancies: the intrinsic redox active sites in metal oxide catalysts, *Advanced Science*, 2020, **7**(2), 1901970, DOI: 10.1002/advs.201901970.

85 S. Soni, V. S. Vats, S. Kumar, B. Dalela, M. Mishra, R. S. Meena and S. Dalela, Structural, optical and magnetic properties of Fe-doped CeO_2 samples probed using X-ray photoelectron spectroscopy, *J. Mater. Sci.: Mater. Electron.*, 2018, **29**(12), 10141–10153, DOI: 10.1007/s10854-018-9060-x.

86 J. Chen, S. Shen, P. Wu and L. Guo, Nitrogen-doped CeOx nanoparticles modified graphitic carbon nitride for enhanced photocatalytic hydrogen production, *Green Chem.*, 2015, **17**(1), 509–517, DOI: 10.1039/C4GC01683A.

87 X. Zou, J. Liu, Y. Li, Z. Shen, X. Zhu, Q. Xia and Y. Wang, Molybdenum-doping promoted surface oxygen vacancy of CeO_2 for enhanced low-temperature CO_2 methanation over Ni-CeO_2 catalysts, *Appl. Surf. Sci.*, 2024, **661**, 160087, DOI: 10.1016/j.apsusc.2024.160087.

88 Y. Mona, Study on the electrochemical performance of Ni-doped ZnO nanorods utilized for the high-performance supercapacitor application, *Ionics*, 2024, **30**(7), 4135–4142, DOI: 10.1007/s11581-024-05588-0.

89 X. Hu, X. Tian, Y. W. Lin and Z. Wang, Nickel foam and stainless steel mesh as electrocatalysts for hydrogen evolution reaction, oxygen evolution reaction and overall water splitting in alkaline media, *RSC Adv.*, 2019, **9**(54), 31563–31571, DOI: 10.1039/C9RA07258F.

90 X. Zou, J. Liu, Y. Li, Z. Shen, X. Zhu, Q. Xia and Y. Wang, Molybdenum-doping promoted surface oxygen vacancy of CeO_2 for enhanced low-temperature CO_2 methanation over Ni-CeO_2 catalysts, *Appl. Surf. Sci.*, 2024, **661**, 160087, DOI: 10.1016/j.apsusc.2024.160087.

91 N. V. Sajith, S. Suresh, M. Bindu, B. N. Soumya, M. P. Kurup and P. Periyat, Visible light active Ni_{2+} doped CeO_2 nanoparticles for the removal of methylene blue dye from water, *Res. Eng.*, 2022, **16**, 100664, DOI: 10.1016/j.rineng.2022.100664.

92 N. T. Suen, S. F. Hung, Q. Quan, N. Zhang, Y. J. Xu and H. M. Chen, Electrocatalysis for the oxygen evolution reaction: recent development and future perspectives, *Chem. Soc. Rev.*, 2017, **46**(2), 337–365, DOI: 10.1039/C6CS00328A.

93 F. Bao, E. Kemppainen, I. Dorbandt, R. Bors, F. Xi, R. Schlatmann and S. Calnan, Understanding the hydrogen evolution reaction kinetics of electrodeposited

nickel-molybdenum in acidic, near-neutral, and alkaline conditions, *ChemElectroChem*, 2021, **8**(1), 195–208, DOI: 10.1002/celc.202001436.

94 M. Tiwari, P. K. Bhartiya, N. Bangruwa, S. K. Sarkar and D. Mishra, Spin polarization and phase transformation-aided efficient overall water splitting using $Ni_{50}Mn_{18}Ga_{25}Cu_7$ ferromagnetic shape memory Heusler alloy, *ACS Appl. Mater. Interfaces*, 2024, **16**(50), 69398–69409, DOI: 10.1021/acsami.4c15932.

95 M. Zhiani and S. Kamali, Synergistic effect of ceria on the structure and hydrogen evolution activity of nickel nanoparticles grown on reduced graphene oxide, *J. Mater. Chem. A*, 2017, **5**(17), 8108–8116, DOI: 10.1039/C7TA00146K.

96 L. Tian, H. Liu, B. Zhang, Y. Liu, S. Lv, L. Pang and J. Li, Ni and CeO_2 nanoparticles anchored on cicada-wing-like nitrogen-doped porous carbon as bifunctional catalysts for water splitting, *ACS Appl. Nano Mater.*, 2021, **5**(1), 1252–1262, DOI: 10.1021/acsanm.1c03850.

97 W. Gao, Z. Xia, F. Cao, J. C. Ho, Z. Jiang and Y. Qu, Comprehensive understanding of the spatial configurations of CeO_2 in NiO for the electrocatalytic oxygen evolution reaction: embedded or surface-loaded, *Adv. Funct. Mater.*, 2018, **28**(11), 1706056, DOI: 10.1002/adfm.201706056.

98 M. Favaro, W. S. Drisdell, M. A. Marcus, J. M. Gregoire, E. J. Crumlin, J. A. Haber and J. Yano, An operando investigation of (Ni–Fe–Co–Ce)Ox system as highly efficient electrocatalyst for oxygen evolution reaction, *ACS Catal.*, 2017, **7**(2), 1248–1258, DOI: 10.1021/acscatal.6b03126.

99 L. Chen, H. Jang, M. G. Kim, Q. Qin, X. Liu and J. Cho, Fe x Ni y/CeO_2 loaded on N-doped nanocarbon as an advanced bifunctional electrocatalyst for the overall water splitting, *Inorg. Chem. Front.*, 2020, **7**(2), 470–476, DOI: 10.1039/C9QI01251F.

100 A. K. Mishra, J. Willoughby, S. L. Estes, K. C. Kohler and K. S. Brinkman, Impact of morphology and oxygen vacancy content in Ni, Fe co-doped ceria for efficient electrocatalyst based water splitting, *Nanoscale Adv.*, 2024, **6**(18), 4672–4682, DOI: 10.1039/D4NA00500G.